A Hierarchy of Global Ocean Models Coupled to CESM1

Tien-Yiao Hsu[1], Francois W. Primeau[2], and Gudrun Magnusdottir[2]

[1]Department of Earth System Science
[2]University of California, Irvine

November 22, 2022

Abstract

We develop a hierarchy of simplified ocean models for coupled ocean, atmosphere, and sea ice climate simulations using the Community Earth System Model version 1 (CESM1). The hierarchy has four members: a slab ocean model, a mixed-layer model with entrainment and detrainment, an Ekman mixed-layer model, and an ocean general circulation model (OGCM). Flux corrections of heat and salt are applied to the simplified models ensuring that all hierarchy members have the same climatology. We diagnose the needed flux corrections from auxiliary simulations in which we restore the temperature and salinity to the daily climatology obtained from a target CESM1 simulation. The resulting 3-dimensional corrections contain the interannual variability fluxes that maintain the correct vertical gradients of temperature and salinity in the tropics. We find that the inclusion of mixed-layer entrainment and Ekman flow produces sea surface temperature and surface air temperature fields whose means and variances are progressively more similar to those produced by the target CESM1 simulation. We illustrate the application of the hierarchy to the problem of understanding the response of the climate system to the loss of Arctic sea ice. We find that the shifts in the positions of the mid-latitude westerly jet and of the Inter-tropical Convergence Zone (ITCZ) in response to sea-ice loss depend critically on upper ocean processes. Specifically, heat uptake associated with the mixed-layer entrainment influences the shift in the westerly jet and ITCZ. Moreover, the shift of ITCZ is sensitive to the form of Ekman flow parameterization.

A Hierarchy of Global Ocean Models Coupled to CESM1

Tien-Yiao Hsu[1], Francois Primeau[1], and Gudrun Magnusdottir[1]

[1]University of California, Irvine, California, United States

Key Points:

- We develop a flux-corrected globally-coupled ocean-model hierarchy that explicitly includes mixed-layer entrainment and Ekman flow.
- The flux corrections need to contain components stemming from the interannual variability to reproduce the vertical gradient of ocean temperature.
- The hierarchy applied with Arctic sea-ice loss reveals that the ITCZ is sensitive to the entrainment and Ekman flow parameterization.

Corresponding author: Tien-Yiao Hsu, `tienyiah@uci.edu`

Abstract

We develop a hierarchy of simplified ocean models for coupled ocean, atmosphere, and sea ice climate simulations using the Community Earth System Model version 1 (CESM1). The hierarchy has four members: a slab ocean model, a mixed-layer model with entrainment and detrainment, an Ekman mixed-layer model, and an ocean general circulation model (OGCM). Flux corrections of heat and salt are applied to the simplified models ensuring that all hierarchy members have the same climatology. We diagnose the needed flux corrections from auxiliary simulations in which we restore the temperature and salinity to the daily climatology obtained from a target CESM1 simulation. The resulting 3-dimensional corrections contain the interannual variability fluxes that maintain the correct vertical gradients of temperature and salinity in the tropics. We find that the inclusion of mixed-layer entrainment and Ekman flow produces sea surface temperature and surface air temperature fields whose means and variances are progressively more similar to those produced by the target CESM1 simulation.

We illustrate the application of the hierarchy to the problem of understanding the response of the climate system to the loss of Arctic sea ice. We find that the shifts in the positions of the mid-latitude westerly jet and of the Inter-tropical Convergence Zone (ITCZ) in response to sea-ice loss depend critically on upper ocean processes. Specifically, heat uptake associated with the mixed-layer entrainment influences the shift in the westerly jet and ITCZ. Moreover, the shift of ITCZ is sensitive to the form of Ekman flow parameterization.

Plain Language Summary

Hierarchies of globally coupled ocean models, meaning adding individual ocean processes progressively, provide valuable understandings of the climate system. One of the difficulties is that surface flux corrections are necessary for reproducing a target climate state. In this paper, we manage to overcome this problem and develop a globally coupled ocean model hierarchy that can turn on and off the processes of mixed-layer entrainment and Ekman flow. We use the hierarchy to study the impact of Arctic sea-ice loss on the climate system. We find that the effect of

mixed-layer entrainment on ocean heat uptake influences the atmospheric circulation by shifting the latitudinal positions of the mid-latitude westerly jet and the Inter-tropical Convergence Zone.

1 Motivation

Model hierarchies contribute to improved understanding of the climate response to external forcing by isolating the influence of various physical processes (e.g., Claussen et al., 2002; Held, 2005; Jeevanjee et al., 2017; Vallis et al., 2018; Maher et al., 2019). While relatively well-developed hierarchies exist for the atmosphere, less effort has been focused on integrating simplified ocean models into global climate models. Inspired by previous regional and intermediate-complexity climate modeling work (Alexander et al., 2000; Haarsma et al., 2005; Alexander & Scott, 2008; Codron, 2012; Hirons et al., 2015), we formulate an ocean-model hierarchy to complement the ocean general circulation model (OGCM) in the Community Earth System Model version 1 (CESM1; Hurrell et al., 2013).

Simplifications of ocean processes in climate models for studies that focus primarily on the atmosphere typically consist of the following options: (1) prescribing the sea surface temperature (SST) (e.g., Magnusdottir and Saravanan 1999), (2) a single, static layer, known as a slab ocean model (SOM), that can take up heat from the atmosphere, store it, and release it back to the atmosphere (Kiehl et al., 2006), and (3) a full OGCM (e.g. POP2; R. Smith et al., 2010). Unlike option (1), the SOM accounts for the finite thermal inertia of the upper ocean. The OGCM, in turn, accounts for the three-dimensional transport of heat by ocean currents that respond dynamically to surface fluxes of heat, freshwater, and momentum. Because the gap between options (2) and (3) is decidedly large, our goal is to formulate two simplified ocean models that narrow the gap between the SOM and the OGCM.

For the first model, we modify the SOM by making the slab thickness a function of time. This time-dependence, which we diagnose from the climatological seasonal cycle in a climate simulation using the OGCM, allows the model to store heat anomalies in the seasonal thermocline where they can be re-entrained into the mixed-layer in the following year. The re-emergence of these heat anomalies creates winter-to-winter SST correlations that are particularly important in the North Atlantic and North Pacific Oceans where they are believed to play an important role in the generation of decadal climate variability (Alexander & Deser, 1995; Alexander et al., 1999, 2000; Kwon et al., 2011; Newman et al., 2016).

In the second model, we add dynamic wind-driven Ekman flows to the previously added time dependence of the mixed-layer depth. The upwelling and downwelling generated by the divergence of these flows provide an additional pathway for the atmosphere to interact with the subsurface ocean. In addition, the Ekman flows contribute to the horizontal transport of heat, which is particularly important in the tropical ocean where it dominates the oceanic heat transport (OHT) (Lee & Marotzke, 1998; Held, 2001). The response of Ekman OHT to changes in surface winds has been shown to be particularly important for damping shifts of the Inter-tropical Convergence Zone (ITCZ) when the Earth is forced with an extra-tropical heat source (Green & Marshall, 2017; Schneider, 2017; Kang, Shin, & Xie, 2018; Kang, Shin, & Codron, 2018; Green et al., 2019).

Despite the relative simplicity of our two new models, we need to address several complications: (1) The linear momentum balance equations used to compute the Ekman flows are singular at the equator. To eliminate the singularity we introduce a Rayleigh friction term. Choosing an appropriate value for the friction coefficient is the first complication. (2) The simplified model with Ekman flow produces a pronounced equatorial rainfall anomaly that originates from a runaway coupled mode along the equator that needs to be damped using an explicit horizontal eddy diffusivity (a mechanistic explanation for this coupled mode is provided in Section 2.6). Choosing an appropriate value for this lateral diffusivity is the second complication that we must address. (3) Finally, because the simplified models neglect many oceanic processes that influence the exchange of heat between the atmosphere and ocean, we need to include prescribed fluxes of heat and moisture in our simplified ocean models to prevent the coupled climate from drifting to unrealistic states. Diagnosing these fluxes is the third complication. We address these complications in Section 2.

In this paper, we illustrate the use of the hierarchy by studying the importance different ocean processes in the response of the climate system to the loss of Arctic sea-ice. Many factors can influence the response, including the background state, wave mean flow interactions in the atmosphere, sea-ice physics, and the exchange of heat with the ocean (Screen et al., 2018; D. M. Smith et al., 2022). Of particular importance for motivating our work is the study of Tomas et al. (2016) that identified the importance of oceanic heat transport for modulating the response of the atmosphere to sea ice loss by comparing simulations performed with an OGCM to simulations with an SOM.

The paper is structured as follows: In Section 2, we introduce the model formulation and solutions to the challenges described above. In Section 3, we investigate the modulating effect of ocean processes on (1) climate variability and (2) the atmospheric response to the loss of Arctic sea ice. In Section 4, we present concluding remarks.

2 Methods

2.1 Hierarchy of ocean models within CESM1

Our hierarchy of climate models is constructed using the Community Earth System Model version 1 (CESM1; Hurrell et al., 2013) by replacing, the standard Parallel Ocean Program version 2 (POP2, henceforth OGCM; R. Smith et al., 2010; Danabasoglu et al., 2012), in turn with three simplified ocean models. These simplified ocean models, which are generated from a unified numerical code written in Julia (`https://github.com/meteorologytoday/EMOM`), consist of a SOM, a mixed-layer model (MLM), and an Ekman mixed-layer ocean model (EMOM). A Julia interface exchanges the surface fluxes with the Fortran CESM1 coupler.

The other components of the climate model consist of the Community Atmosphere Model version 4 (CAM4; Neale et al., 2013), the Los Alamos Sea Ice Model version 4 (Hunke et al., 2010), Community Land Model version 4 (Lawrence et al., 2011), and the River Transport Model (as part of Community Land Model). This configuration of the climate model is equivalent to the Community Climate System Model 4 (CCSM4; Gent et al., 2011).

All the simulations are run with nominally $1^\circ \times 1^\circ$ horizontal resolution: The atmosphere and land models have 192 and 288 points in latitude and longitude on a Gaussian grid (also termed f09 in CESM1). The ocean and sea-ice models have 384 and 320 points in latitude and longitude with a displaced-pole grid (also termed g16 in CESM1).

2.2 Oceanic general circulation model (OGCM)

The Parallel Ocean Program version 2 (POP2) used in our study has a nominal horizontal resolution of about $1^\circ \times 1^\circ$. However, the meridional resolution between 10°S and 10°N — the range within which ITCZ shifts occur — is better than 0.27° of latitude. Furthermore, the grid's "North Pole" is displaced to sit in Greenland, thus avoiding any polar coordinate singularity in the ocean (R. Smith et al., 2010). In the vertical, the model has 60 levels with separation ranging from 10 m in the top 160 m of the water column, increasing monotonically from 10m to 250 m in the depth range between 160 m, and 3500 m, and is fixed at 250 m down to the maximum ocean depth of 5500 m. The model's mixed-layer dynamics are governed by the K-profile parameterization (KPP) vertical-mixing scheme (Large et al., 1994). The model also uses the Gent and McWilliams (1990) isopycnal mixing scheme.

2.3 Ekman mixed-layer ocean model (EMOM)

The unified code for our hierarchy of simplified ocean models is called EMOM. We show the physical processes that are represented by EMOM in schematic form in Figure 1. EMOM is coupled to the other climate model components through the CESM coupler. EMOM has 33 vertical layers identical to the top 33 layers of the POP2 configuration. These 33 layers cover a total depth ≈ 503.7 m and range in thickness from 10 m to 48 m. EMOM solves the following equations governing the time-evolution of temperature, T, and salinity, S,

$$\frac{\partial T}{\partial t} + \vec{\mathbf{v}}_H \cdot \nabla_H T + w\frac{\partial T}{\partial z} = \frac{\partial}{\partial z}\left(K_V \frac{\partial T}{\partial z}\right) + \nabla_H \cdot (K_H \nabla_H T) - \frac{1}{\rho c_p}\frac{\partial F_T}{\partial z} - \frac{1}{t_R}(T - T_{\text{clim}}) - \frac{\Lambda}{\tau_{\text{FRZ}}}(T - T_{\text{FRZ}}) + \frac{Q_T}{\rho c_p}, \tag{1a}$$

$$\frac{\partial S}{\partial t} + \vec{\mathbf{v}}_H \cdot \nabla_H S + w\frac{\partial S}{\partial z} = \frac{\partial}{\partial z}\left(K_V \frac{\partial S}{\partial z}\right) + \nabla_H \cdot (K_H \nabla_H S) - \frac{\partial F_S}{\partial z} - \frac{1}{t_R}(S - S_{\text{clim}}) + Q_S, \tag{1b}$$

where $\rho = 1026$ kg/m^3 and $c_p = 3996$ J/K/kg are the density and heat capacity of seawater, F_T is the energy flux consisting of radiation, sensible, and latent heat fluxes, F_S is the virtual salt flux to account for evaporation minus precipitation, runoff, sea-ice melting and brine injection, $\vec{\mathbf{v}}_H$ is the horizontal velocity, w is the vertical velocity component, h is the mixed-layer thickness, Q_T and Q_S are heat and salt flux correction terms, ∇_H is the horizontal gradient or divergence operator, K_H is the horizontal diffusivity. K_H depends on latitude according to

$$K_H = K_0 + (K_1 - K_0)\exp\left(-\frac{\phi^2}{2\sigma_K^2}\right)\exp\left(\frac{z}{H_K}\right) \tag{2}$$

with ϕ is the latitude in radians, $K_0 = 5.0 \times 10^3\,\mathrm{m^2/s}$, $K_1 = 2 \times 10^4\,\mathrm{m^2/s}$, $\sigma_K = 2\pi/36$ (= 10°) and $H_K = 100\,\mathrm{m}$. The value of K_0 is referenced from Nummelin et al. (2021) in which the SST diffusivity is diagnosed (see their Figure 2). The values of K_1 and σ_K are chosen to prevent the spurious rainfall pattern mentioned in the introduction and further discussed in Section 2.6. K_V is the vertical diffusivity that depends on the mixed-layer thickness and vertical gradient of buoyancy, b. Explicitly,

$$K_V = \begin{cases} 1\ \mathrm{m^2/s} & \text{if } -h < z < 0 \text{ or } \frac{\partial b}{\partial z} < 0, \\ 1 \times 10^{-4}\,\mathrm{m^2/s}, & \text{otherwise.} \end{cases} \tag{3}$$

The short-wave radiative heating is divided into two components and each follows an exponential depth profile with a constant e-folding depth. The parameters are selected according to Type I water in Table 2 of Paulson and Simpson (1977). The remaining surface heat fluxes and virtual salt fluxes are implemented as interior sources in the top 10-meter-thick layer of the model so that Equations (1a) and (1b) can be solved subject to no-flux boundary conditions.

To compute the buoyancy, we approximate the density using a third-order polynomial approximation for the equation of state as described in Bryan and Cox (1972). In the numerical implementation, K_V is specified at the interface between the grid boxes. The effective mixed-layer thickness must therefore coincide with the discrete depths of the interfaces between the grid boxes. T_{clim} and S_{clim} are the 50-year reference monthly climatological profiles that the entire ocean is weakly restored to with a timescale $t_R = 100$ years. With this choice of t_R, we refer to this term as the “weak-restoring” term. To take into account the latent heat exchanges associated with the transformation of water between the liquid and solid phases, we introduce the parameters $\tau_{\mathrm{FRZ}} = 1\,\mathrm{day}$ and $T_{\mathrm{FRZ}} = -1.8°\mathrm{C}$ as the freezing timescale and freezing point of ocean water. Λ is the Heavyside step function, i.e.,

$$\Lambda = \begin{cases} 1 & \text{if } T < T_{\mathrm{FRZ}}, \\ 0 & \text{otherwise.} \end{cases}$$

This design switches on the freezing process so that ocean temperature is forced to be above the freezing point. The latent heat released is sent to the coupler so that sea ice may grow. For simplicity, we prescribe the space and time dependence of h. We considered adopting a dynamic mixing layer model such as the KPP scheme (Large et al., 1994) as used in the POP2 model or a Niiler-Kraus type bulk formulation (Niiler, 1977; Gaspar, 1988). However, the former needs as input the vertical sheer, which is not available in our simplified model, and the latter, which we implemented and tested, produces a mean mixed-layer thickness that is substantially different than the one in the parent simulation. This difference in the mean state complicates the interpretation of our experiments. For these reasons, we focus here on the simplified models with a prescribed time-dependence for the mixed-layer thickness.

As for the velocity field, we use the the same formulation as Codron (2012) in which the Ekman velocity is diagnosed from the instantaneous wind-stress using a linear momentum balance:

$$\vec{\mathbf{v}}_{\mathrm{EK}} = \frac{1}{\rho H_{\mathrm{EK}}(\epsilon^2 + f^2)} \left(f\tau^y + \epsilon\tau^x, -f\tau^x + \epsilon\tau^y \right) \tag{4}$$

where $H_{\mathrm{EK}} = 50\,\mathrm{m}$ is the Ekman layer thickness, f the latitude-dependent Coriolis parameter, and $\vec{\tau} = (\tau^x, \tau^y)$ is the surface wind stress, ϵ the Rayleigh friction coefficient that removes the singularity of Ekman solution at the equator. The value of ϵ is set to $\epsilon = 1.4\times10^{-5}\,\mathrm{s}^{-1}$ (see Section 2.4 for detail) so that the Rayleigh friction dominates over the Coriolis force in a narrow band between 5.5°S and 5.5°N. At the equator $\vec{\mathbf{v}}_{\mathrm{EK}}$ becomes aligned with the direction of surface wind stress. We will call the part of $\vec{\mathbf{v}}_{\mathrm{EK}}$ that is proportional to $\epsilon\vec{\tau}$ the frictional Ekman flow.

Two alternative parameterizations have been proposed for removing equatorial Ekman-balance singularity. In terms of the cross-equatorial ocean heat transport, these parameterizations produce a better agreement between the OGCM and the simplified ocean model. However, there are other problems with these alternative parameterizations. The parameterization of Kang, Shin, and Codron (2018) drops the ϵ term in the numerator of the second component of Equation (4). Unfortunately, this simplification cannot be justified from the original momentum equation. In order to drop the ϵ dependence in the numerator of the meridional component of Equation (4), the Rayleigh friction term in the zonal momentum equation must vanish, but without it, the zonal component of Equation (4) would still be singular at the equator. The other parameterization (Afargan-Gerstman & Adam, 2020) was proposed in the context of an aqua-planet simulation where the zonal symmetry causes the mean meridional wind component to vanish so that only the meridional Ekman flow needs to be considered. For this special case, the Ekman-balance singularity can be eliminated by retaining the latitudinal-dependence of the Coriolis parameter, i.e. the β effect, and noting that in the absence of friction the meridional Ekman flow is proportional to the curl of the wind stress divided by β. No such balance is available for the zonal Ekman flow, which will still be singular if it is present. Because we are considering a realistic continental configuration, we decided to adopt Codron's original formulation, i.e. Equation (4).

As in Codron (2012), we put the return flow directly below the Ekman layer with a volume flux in the opposite direction and of equal magnitude to the surface Ekman flow. That is,

$$\vec{\mathbf{v}}_{\mathrm{RF}} = -\frac{H_{\mathrm{EK}}}{H_{\mathrm{RF}}}\vec{\mathbf{v}}_{\mathrm{EK}}, \tag{5}$$

where $H_{\mathrm{RF}} \approx 453.7\,\mathrm{m}$ is the thickness of the return flow so that the resulting thickness conveniently coincides with OGCM grid. Thus the horizontal velocity is $\vec{\mathbf{v}}_{\mathrm{EK}}$ $z \in (-H_{\mathrm{EK}},0]$ and $\vec{\mathbf{v}}_{\mathrm{RF}}$ for $z \in (-(H_{\mathrm{EK}}+H_{\mathrm{RF}}), -H_{\mathrm{EK}}]$. This parameterization ensures that the vertically integrated $\vec{\mathbf{v}}_{\mathrm{EK}}$ is zero.

The resulting Ekman OHT is easy to diagnose given the temperature profile in each water column. For any given water column, Ekman OHT is given by

$$\begin{aligned}
\mathrm{OHT}_{\mathrm{EK}} &= \rho_0 c_p \int_{z=-(H_{\mathrm{EK}}+H_{\mathrm{RF}})}^{0} v_{\mathrm{EK}} T \,\mathrm{d}z \\
&= \rho_0 c_p \left(H_{\mathrm{EK}} v_{\mathrm{EK}} T_{\mathrm{EK}} + H_{\mathrm{RF}} v_{\mathrm{RF}} T_{\mathrm{RF}}\right) \\
&= c_p \Delta T \left(\frac{-f\tau^x + \epsilon\tau^y}{\epsilon^2 + f^2}\right)
\end{aligned} \tag{6}$$

where

$$T_{\mathrm{EK}} = \frac{1}{H_{\mathrm{EK}}} \int_{-H_{\mathrm{EK}}}^{0} T \,\mathrm{d}z, \text{ and } T_{\mathrm{RF}} = \frac{1}{H_{\mathrm{RF}}} \int_{-(H_{\mathrm{EK}}+H_{\mathrm{RF}})}^{-H_{\mathrm{EK}}} T \,\mathrm{d}z \tag{7}$$

are the mean temperatures over the Ekman and return-flow layers, and

$$\Delta T \equiv T_{\mathrm{EK}} - T_{\mathrm{RF}} \tag{8}$$

is the difference between the mean temperatures defined above. In going from the second to the third line of Equation (6), we used Equation (5). Given typical tropical wind stress $(\tau^x, \tau^y) = (0.01, 0)\mathrm{N/m^2}$ at latitude 5.5°N where $\epsilon = f$ (Section 2.4 shows how we pick ϵ), the computed zonally integrated ($2\pi \cos 5.5^\circ \times$ (Radius of earth) $\approx 4 \times 10^7$m) meridional OHT is about 0.06 PW per °C change of ΔT.

On the numerical side, EMOM is discretized using Arakawa C-grid. The model exchanges surface fluxes with the atmosphere every 24 hours. The time step is set to three hours. Advection and horizontal diffusion are implemented using the QUICKEST scheme (upwind, second-order accuracy; Leonard, 1979). Finally, the vertical diffusion, weak-storing, and freezing process are solved using the implicit Euler backward method.

All the members of our hierarchy except for the OGCM can be recovered from the same code base. To recover the MLM, we simply set $\vec{\mathbf{v}} = 0$. To recover the SOM, we (i) set $\vec{\mathbf{v}}_H = \mathbf{0}$, (ii) set the mixed-layer thickness of each grid point to its time-averaged value, and (iii) replace the topography mask to match the time-averaged mixed-layer thickness. With these settings, $w_e = 0$ and $K_v = 1$ m^2/s everywhere, which makes our model equivalent to a well-mixed slab.

There are two major differences between CESM1-SOM and our SOM. First, CESM1-SOM sets the horizontal diffusivity K_H to zero while our SOM has non-zero spatially varying K_H given by Equation (2). This choice simplifies the task of comparing the output of the different models of our hierarchy. Second, the CESM1-SOM uses the boundary layer depth output from POP2 (variable `HBLT`) instead of mixed-layer depth (variable `HMXL`), which we use in EMOM, for the mixed-layer thickness. The boundary layer depth and the mixed-layer thickness are equal when they are at their maximum, but otherwise the boundary layer is thinner than the mixed-layer. Past studies have shown that a shallower annual-mean mixed-layer thickness leads to colder SSTs, which tends to increase the albedo through cloud-radiative feedback processes (Donohoe et al., 2014; Wang et al., 2019). However, the flux corrections that are applied to our simplified models will generally eliminate this effect on the mean climate. The choice of thickness would most likely also affect the climate variability, but the above mentioned studies do not offer any specific recommendation as to which choice is preferable in a SOM. We, therefore, chose to set h to `HMXL`.

The full OGCM completes our hierarchy as the most realistic ocean model. Thus, the resulting hierarchy of ocean models from simplest to most complex are: the SOM, the MLM, the EMOM, and the OGCM. As we progress up the hierarchy the MLM includes entrainment, which is absent in the SOM, the EMOM includes Ekman transport, which is absent in the MLM and the OGCM includes everything else (i.e. gyres, overturning circulation, waves, etc.)

2.4 Estimation of Rayleigh Friction ϵ in Equation (4)

To avoid the singularity of the Ekman flow solution at the equator, we introduced a Rayleigh friction term in the horizontal momentum equations used to derive Equation (4). To determined the value of ϵ, we minimized the sum of the squared differences between the vertical velocities computed by the OGCM and those computed from the divergence of $\vec{\mathbf{v}}_{\mathrm{EK}}(\epsilon)$ integrated from the surface, assumed flat and rigid, down to a depth of $H = 50$ m in the latitude band between 10°S–10°N. Explicitly,

$$\epsilon = \underset{\epsilon}{\operatorname{argmin}} \sum_{i \in \mathcal{X}} \left| w^i_{\mathrm{OGCM}} - w^i_{\mathrm{EK}}(\epsilon) \right|^2 \tag{9}$$

where

$$w^i_{\mathrm{EK}}(\epsilon) = H \nabla \cdot \vec{\mathbf{v}}_{\mathrm{EK}}(\epsilon), \tag{10}$$

and $\mathcal{X}$ denotes the set of mesh points between 10°S and 10°N.

The solution to the above non-linear least-squares problem yielded a value of $\epsilon = 1.4 \times 10^{-5}\ \mathrm{s}^{-1}$. With this choice for ϵ, Rayleigh friction dominates over the Coriolis force between 5.5°S–5.5°N. Thus within 5° of the equator, the Ekman flow is more parallel than perpendicular to the direction of the wind stress. At the equator, the Ekman flow is exactly aligned with the wind stress.

2.5 Derivation of correction flux

For the simulations that use SOM, MLM, and EMOM, we apply flux corrections to force the simulated climates towards the one simulated using CESM1 (i.e. CTL_OGCM; see Section 2.7). The flux corrections make up for the mean heat and freshwater transports captured by the full OGCM but not explicitly represented in our simplified models. These flux corrections include rectification effects due to interanual variability. For example, if we decompose the variables in Equation (1a) into a mean annual cycle plus anomaly, i.e. $(\cdot) = \overline{(\cdot)} + (\cdot)'$, and then apply the averaging operator $\overline{(\cdot)}$, we obtain

$$\begin{aligned} \frac{\partial \overline{T}}{\partial t} + \overline{\vec{\mathbf{v}}}_{\text{EK}} \cdot \nabla_H \overline{T} + \overline{w}_{\text{EK}} \frac{\partial \overline{T}}{\partial z} &= \frac{\partial}{\partial z}\left(K_V \frac{\partial \overline{T}}{\partial z}\right) + \nabla_H \cdot \left(K_H \nabla_H \overline{T}\right) - \frac{1}{\rho c_p}\frac{\partial \overline{F}_T}{\partial z} - \frac{1}{t_R}\left(\overline{T} - T_{\text{clim}}\right) \\ &- \frac{\overline{\Lambda}}{\tau_{\text{FRZ}}}\left(\overline{T} - T_{\text{FRZ}}\right) + \left[\frac{\overline{Q}_T}{\rho c_p} - \overline{\vec{\mathbf{v}}'_{\text{EK}} \cdot \nabla_H T'} - \overline{w'_{\text{EK}} \frac{\partial T'}{\partial z}} + \overline{K'_V \frac{\partial^2 T'}{\partial z^2}} - \frac{\overline{\Lambda' T'}}{\tau_{\text{FRZ}}}\right]. \end{aligned} \tag{11}$$

The terms in the square bracket correspond the flux corrections needed to reproduce the mean annual cycle. In addition to the effect of missing processes, $\overline{Q_T}$, the bracket includes anomaly-product terms. Some of the interannual variability that produces the anomalies that contribute to these product terms will be generated spontaneously by the simplified models. Their effects do not need to be included in the flux correction. However, some of the interannual anomalies originate from processes that can only be simulated using the full OGCM and will, therefore, be absent in our simplified climate models. As a prominent example, the El Niño-Southern Oscillation (ENSO), which dominates in the tropics, cannot be captured in our simplified models. Its effect on the annual mean fluxes must be included as part of the flux correction. Without it, our models cannot reproduce the correct vertical temperature gradient. There is, however, a potential risk of double-counting the effect of anomalies that can simulated in the simplified coupled climate models.

To derive the flux correction given by the terms in the square bracket of Equation (11), we first use the 50-year daily climatology of temperature and salinity (T_{clim} and S_{clim}) from the end of a 1000-year spin-up run. Then, for each model, we temporarily set $t_R = 15\,$days in the simplified model and run the resulting coupled climate model for 20 years. We then record the monthly mean values of the restoring term for the last 19 years. Finally, we average each month to produce a three-dimensional flux correction that is periodic with a period of one year.

2.6 Importance of large K_H near the equator

Without explicit horizontal diffusion, EMOM produces a persistent band of excessively strong equatorial precipitation in the Central Pacific (Figure S1a, 150-170°W with the zonal mean shown in Figure S1b).

In a narrow band along the equator where the frictional force dominates over the Coriolis, convergent surface winds (Figure S1b, red dashed line) above a warm SST anomaly (Figure S1c, black solid line) also drive convergent ocean currents that suppress upwelling (Figure S1c, red dashed line). Off the equator, where the Coriolis force dominates over the friction force the wind-driven currents are divergent and drive upwelling. Further examination of the meridional wind stress τ^y and ocean 50-m vertical velocity $w_{50\mathrm{m}}$ reveals that this is a consequence of the following coupled positive feedback. Since our Rayleigh friction dominates over the Coriolis force within 5.5° of the equator, anomalous wind convergence drive anomalous SST convergence near the equator. The resulting warming of the sea surface acts to reinforce the convection in the overlying atmosphere. Furthermore, the upwelling of cold waters in regions straddling the center of atmospheric convection induces locally descending motion in the atmosphere, which acts to further reinforce the the convergent winds and atmospheric convection.

In the real ocean, the generation of the strong temperature gradients seen in Figure S1c would lead to a baroclinic instability that would generate a vigorous eddy field. The diffusive fluxes generated by these eddies would come to balance the advective flux due to the mean flow. By positing a balance between the advective and diffusive fluxes, we can estimate an appropriate value of K_H so that we can suppress the spurious rain band in EMOM,

$$K_H \frac{\partial^2 T}{\partial y^2} = -v \frac{\partial T}{\partial y} \tag{12}$$

$$\Rightarrow K_H \approx |v \Delta y| \tag{13}$$

where Δy is the meridional length scale. From Figure S1 we estimate that $\Delta y \approx 400\,\mathrm{km}$, and that the maximum meridional ocean Ekman flow is about $\max(|\tau^y|)/(\rho_0 \epsilon\, 50\,\mathrm{m}) \approx 0.028\,\mathrm{m}/\mathrm{s}$. From these scales, we estimate $K_H = |v\Delta y| = 1.12 \times 10^4\,\mathrm{m}^2/\mathrm{s}$. Thus, to ensure the suppression of coupled positive feedback, we set K_1 in Equation (2) to be $2 \times 10^4\,\mathrm{m}^2/\mathrm{s}$.

2.7 Simulation design

Since we want to test how ocean processes modulate climate variability and the response to Arctic sea-ice loss, it is necessary to have a set of control runs where all hierarchy members produce the same climate.

The control runs are initialized with the January-mean fields from the end of the 1000-year spin-up simulation with the full OGCM. They are performed with the necessary correction fluxes derived in Section 2.5 and are labeled as CTL_[MODEL] where [MODEL] can be one of SOM, MLM, EMOM, or OGCM. The CTL simulations are run for 120 years and the last 100 years are analyzed. The biases of each model are defined as the deviations from the CTL_OGCM simulation as opposed to the observed mean state.

The perturbation runs are performed with projected Arctic sea-ice loss such that sea-ice thickness matches the mean sea-ice thickness of the year 2081–2100 of RCP8.5 simulation. The details of how the forcing is applied are explained in Appendix A. As we did for the CTL runs, the sea-ice-loss runs are denoted by SIL_[MODEL]. Also, we denote the entire set of sea-ice-loss runs as SIL and define RESP_[MODEL] := SIL_[MODEL] − CTL_[MODEL].

SIL is run for 180 years. SIL_SOM quickly reaches equilibrium within 50 years whereas the rest of the models adjust quickly in the first 80 years and slowly drift afterward (Figure S2a). In SIL_OGCM, the AMOC weakens during the first 30 years followed by a recovery during the next 50 years, and then stabilizes (Figure S2b). Therefore, we analyze years 81–180 and use this period to represent the decadal and centennial adjustment of the climate system.

3 Results

3.1 Assessment of the mean states

This section presents the analysis of the CTL runs. The experimental setup is documented in Section 2.7.

The simulated climates agree more with the CTL_OGCM as we include more ocean processes. We here discuss the sea-ice and SST biases as they are two important surface properties that control the climate.

3.1.1 Sea-ice area is better constrained than sea-ice volume

For each CTL simulation with a simplified ocean model, we compared the simulated sea-ice area and the sea-ice volume to the area and volume simulated using the OGCM. The results are summarized in Table 1. The relative sea-ice area biases range from -15% to +2%, while the relative sea-ice volume bias is -30% to +3%. We find a smaller bias for the area compared to the volume in both hemispheres. This larger bias for the volume compared to the area is due to latent heat fluxes in the presence of sea ice that are invisible to our method for diagnosing the flux corrections – recall that our flux corrections are diagnosed from a restoring term that acts on the water temperature (Section 2.5).

Another possible reason for sea-ice biases is the double-counting of the $\overline{\Lambda' T'}$ term in Equation (11), as discussed in Section 2.5. In high latitudes, an important role of the ocean is to serve as a heat reservoir, meaning that the SOM can produce a portion of the interannual variability. Since lower ocean temperature activates the freezing, Λ' and T' are negatively correlated, i.e., $\overline{\Lambda' T'} < 0$. Therefore, if the term $\overline{\Lambda' T'}$ is a significant contributor to the flux correction and a significant fraction of $\overline{\Lambda' T'}$ in the CTL_OGCM, including the associated heat fluxes contributes to the warm SST biases we see in Figure 2.

3.1.2 Entrainment reduces SST bias

In all simplified models, the SST biases in most of the regions are within 0.5°C (Figure 2). The biases in the CTL_SOM have a similar pattern to those obtained using the CCSM3-SOM (c.f. Figure 2 of Bitz et al., 2012): warmer SSTs over the tropical Eastern Pacific and the Southern Ocean and colder SSTs along the Kuroshio Extension. Once the mixed-layer dynamics are included, these biases are significantly reduced. The tropical warm bias in CTL_SOM causes more precipitation than CTL_MLM and CTL_EMOM (Figure 3).

The common warm SST bias regions are along the sea-ice edge in the Southern Ocean, with CTL_EMOM having the largest bias. This contradicts our expectation that SST bias should decrease as more ocean processes are included. Since the location of this warm SST bias is along the sea-ice edge, it might due the double-counting of $\overline{\Lambda' T'}$ the same issue as discussed in the previous section on sea-ice bias.

3.2 The impact of ocean processes on variability

Even though hierarchy members produce a similar climate mean states, their variability may differ. Here, we define "variability" as the standard deviation of the anomaly time series of the given variable. The anomaly is the deviation from its climatology (monthly, seasonally, or annually depending on the context).

We also examine the "re-emergence" of SST anomaly (SSTA). It refers to the 12-month lag correlation of SSTA in winter (Alexander et al., 2000). This memory effect is a consequence of seasonal mixed-layer entrainment, which leads to enhanced predictability.

3.2.1 Variability of SST and surface air temperature is improved

Because our simplified models cannot generate most of the tropical variability due to the lack of Kelvin and Rossby waves dynamics, direct comparison between full OGCM with the simplified models would be harder to interpret. Thus, we define CTL_OGCM* as the filtered CTL_OGCM in which we subtract out the projection of the variability on the first empirical orthogonal function of the monthly SSTA between 20°S–20°N.

In general, the SST variability is similar to that of CTL_OGCM*, with higher variability along the storm track (Figure 4). We also notice that SST variability decreases by about 10~30% in CTL_MLM and CTL_EMOM compared to CTL_SOM (Figure 4) even though they have similar atmospheric variability (sea-level pressure, not shown). Since CTL_SOM does not have mixed-layer entrainment, it highlights the importance of the seasonal entrainment in winter that acts to dampen the stochastic atmospheric forcing. We further verify that mixed-layer entrainment can effectively reduce the SST variability by constructing a stochastic one-dimensional mixed-layer model in Appendix B.

Once we include the Ekman flow, the shape of the SST variability pattern in the simplified model of certain regions resembles more to that in the OGCM (Figure 4). These regions are Northern Pacific (box A), Northern Atlantic (box B), and Pacific-Atlantic sector of Southern Ocean (box C). In particular, the tongue-shaped SST variability pattern extending eastward from Japan (box A) in CTL_EMOM resembles the pattern of Pacific Decadal Oscillation (PDO) SST variability. Since we cannot observe this in CTL_SOM and CTL_MLM, it shows that Ekman is an essential process reshaping SST variability pattern. This is consistent with Newman et al. (2016) that a portion of PDO SST variability originates from coupled effect of the weather noises with Ekman flow. Our hierarchy conveniently demonstrate this effect. Besides, the magnitude of the SST variability in box A is not as strong as the variability in CTL_OGCM*, implying that the Kuroshio Extension variability, which is not captured in our simplified models, is an important contributor of SST variability in the North Pacific. Similarly, the reduced SST variability bias is accompanied by a reduction in winter surface-air-temperature variability. In the Southern Ocean (Figure. 5 box A), both mixed-layer entrainment and Ekman flow reduce the biases. In North America (box B), including Ekman flow reduces the bias, likely because it locates downstream of the regions where SST variability biases are reduced.

3.2.2 SSTA re-emergence improvement

In CTL_OGCM, we find stronger re-emergence signals in higher latitudes during winter, specifically in the North Pacific (Figure 6 box A) and Southern Ocean (Figure 6 box B). While the re-emergence bias is reduced in the North Pacific (box A), it is too strong in the Southern Ocean (box B). We speculate that in the Southern Ocean, the northward transport of the subducted Antarctic Intermediate Water and diffusive effect of eddies remove much of the signal that leads to low winter-to-winter correlation in the CTL_OGCM. Without these processes, winter-to-winter correlation will be too strong.

In all simplified models, a strong winter-to-winter correlation is present in the tropical Eastern Pacific while there is none in CTL_OGCM (Figure 6 box C). Although we are unsure of the causes to the low winter-to-winter correlation in CTL_OGCM, we speculate that it is due to the presence of the horizontal currents and wave dynamics that might act to damp the temperature anomalies.

3.3 Response to sea-ice loss

This section presents the analysis of the response of climate to Arctic sea-ice loss during year 81–180. The experiment detail is documented in Section 2.7.

3.3.1 Roles of entrainment and AMOC slowdown in ocean heat uptake

All the models in the hierarchy show a significant SST warming in the northern hemisphere due to Arctic sea-ice loss forcing (Figure 7), whereas the southward extent of the warming gets weaker as more ocean processes are included. In the North Pacific, the southward extent of the warming in RESP_EMOM is similar to RESP_OGCM, especially the warm SST tongue in the center. In contrast, in the North Atlantic the decrease of SST in RESP_OGCM, also known as the “SST warming hole”, is not simulated in any of the simplified models. The warming hole in RESP_OGCM seems to reduce the warming extent over the North Pacific as well.

The warming extent of SST in SOM is the largest, which is consistent with the fact that the SOM traps the heat in the ocean surface layer. Furthermore, including mixed-layer entrainment and Ekman flow is insufficient to reproduce the reduced extent of warming in the North Atlantic of RESP_OGCM. The SST warming is better captured in the North Pacific than in the North Atlantic in our simplified models. Since AMOC responds strongly to sea-ice loss (Figure S2b), we speculate that AMOC in the OGCM efficiently removes the anomalous heat after being transferred to the subsurface in the Atlantic. The role of the AMOC slowdown can be understood from the rough alignment of the anomalous AMOC upwelling (Figure 8) with the latitudinal location of the SST warming hole in RESP_OGCM (Figure 7) between 40°N–60°N. The slowdown of AMOC creates an anomalous heat flux divergence between 40°N–60°N that removes the anomalous heat entrained from the surface. Thus, the efficient ocean heat uptake in RESP_OGCM is a combined effect of entrainment and AMOC slowdown.

3.3.2 The response of the position of westerly jet is sensitive to ocean heat uptake

The atmospheric zonal mean temperature response to Arctic sea-ice loss aligns latitudinally with the warming response in the ocean in all the models (Figure 9). The horizontal and vertical extent of the warming decreases as we include more ocean processes. Since the response follows the thermal wind relation (not shown), we can use the resulting different meridional gradients of the zonal mean temperature to explain the mean jet response. For example, we see that in RESP_SOM, the atmospheric warming is so extensive that it reduces the meridional temperature gradients on both sides of the westerly jet, resulting in an overall weakening of the jet. The gradients in RESP_MLM and RESP_EMOM over the northern edge of the jet decrease much more than to the south, which weakens the westerly jet and shifts it southward. Furthermore, in RESP_OGCM the temperature gradient is decreased to the north but increased to the south such that the jet is shifted rather than weakened. We conclude that the response of the westerly jet to sea-ice loss is sensitive to ocean processes that take up the heat.

3.3.3 The response of ITCZ position is sensitive to surface ocean processes

The response of tropical precipitation to Arctic sea-ice loss highlights the connection between sea-ice loss and ITCZ shifts (Figure 10). The ITCZ shifts northward, into the warmed hemisphere, in all models but with various extents and shapes. In RESP_SOM, there is a significant northward shift of ITCZ across the globe and this signal is reduced in RESP_MLM and amplified in RESP_EMOM. Note that RESP_OGCM shows a moderate ITCZ shift in the Atlantic Ocean and mostly a narrowing of the rainband towards the equator in other basins.

The shift in the ITCZ is a consequence of the excessive energy that is injected into the Arctic and transported across the equator into the southern hemisphere. This anomalous planetary heat transport (PHT) is partitioned into atmosphere heat transport (AHT) and OHT. The ITCZ shift is correlated with the anomalous AHT (Schneider et al., 2014). Here, we expect that the ITCZ shift may be suppressed in two ways: by (1) ocean heat uptake, or (2) southward cross-equatorial OHT through Ekman flow.

The first case, ocean heat uptake, applies to RESP_MLM and RESP_OGCM. Comparing the zonal mean of precipitation response of RESP_MLM to RESP_SOM (Figure 11), we see that RESP_MLM and RESP_SOM peak at the same latitude on the northern side but RESP_MLM is only half the strength. This is because the heat is sent to the subsurface through the entrainment and temporarily reduces the imbalance of inter-hemispheric energy budget. Since RESP_OGCM takes up the heat even more efficiently with the aid of anomalous AMOC, its ITCZ shift is the weakest (Figure 10).

The second case, Ekman modulation, stems from the physical argument that the response of zonal wind stress in both hemispheres drives a southward Ekman OHT (Schneider, 2017; Green & Marshall, 2017; Green et al., 2019; Kang, 2020; Adam, 2021). However, our simulation RESP_EMOM shows the opposite. While weakened trade winds in the northern hemisphere and strengthened trade winds in the southern hemisphere (Figure 12 solid line) should produce southward Ekman OHT, the northward wind stress on the equator (dashed line) generates a northward OHT. The net result of these two regimes drives heat convergence (divergence) in the northern (southern) hemisphere resulting in amplified northward ITCZ shift.

To understand the apparent inconsistency between the amplified ITCZ shift in RESP_EMOM and the expectation from past studies arguing that Ekman flow should damp the shift, we examine the Ekman OHT, i.e. $\mathrm{OHT_{EK}}$ defined in Equation (6). $\mathrm{OHT_{EK}}$ has two contributions, one from $-f\tau^x$ and the other from $\epsilon\tau^y$. Past studies omitted the contribution from $\epsilon\tau^y$. However, there is evidence from OGCM simulations for the existence of the frictionally-driven overturning. For example, Figure 9 of Jayne and Marotzke (2001) shows a shallow frictionally driven Ekman overturning cell within the top 100m of the ocean surface. Also, a shallow clockwise overturning cell near the surface at the equator that is superimposed onto the deeper and stronger counterclockwise density-driven overturning cell is also shown in Figure 5c and 5f of Green et al. (2019). Although the frictionally-driven cell is poorly resolved, its effect on the OHT is visible in Figure 9b of Green et al. (2019). The bump in the OHT-v.s.-latitude plot at the equator is a manifestation of the anomalous frictionally-driven Ekman heat transport. However, Equation (6) also shows that $\mathrm{OHT_{EK}}$ is proportional to ΔT, which can be directly modified by the choice of $H_{\mathrm{total}} = H_{\mathrm{EK}} + H_{\mathrm{RF}}$, the total thickness for the Ekman and return flows. As a result, our simplified model could potentially sensitive to the choices of H_{EK} and H_{RF}.

We summarize this discussion in Figure 13 that shows the decomposition of the heat transport in each model. In the RESP_SOM and RESP_MLM, almost all the response is through AHT with a small contribution to OHT. The contribution to OHT due to diffusion is small. The AHT in RESP_MLM is smaller than for RESP_SOM because the ocean takes up the heat. In RESP_OGCM, the ocean takes up heat and also transports it horizontally so that the subsurface cold water can be replenished to efficiently take up the heat. In RESP_EMOM, the OHT at the equator is northward due to frictional Ekman flow, resulting in an amplification of the ITCZ shift.

4 Conclusion

In this paper, we constructed a hierarchy of ocean models including SOM, MLM, EMOM, and OGCM (POP2) that separates mixed-layer entrainment and Ekman flow by progressively including each process into the model. We further couple it to the climate model CESM1 with realistic topography and successfully derive three-dimensional correction flux through the nudging method so that the appropriate climatologies for SST, precipitation, and sea-ice area are reproduced.

The mixed-layer entrainment is important for multiple reasons. In the control climate, we found that mixed-layer entrainment significantly reduces the SST bias in SOM. The entrainment also reduces SST variability that is exaggerated in SOM, since it introduces cold deep water into the mixed-layer during winter when interannual variability is the strongest. Entrainment also results in stronger winter-to-winter SSTA correlation in agreement with the OGCM almost everywhere. There are, however, two prominent exceptions. In the Southern Ocean and tropical Eastern Pacific, the simplified models produce too high winter-to-winter SSTA correlations. Because horizontal transport would remove local temperature anomalies, we speculate that the high correlation is due to their absence in the simplified models. In the sea-ice loss perturbation experiment, including entrainment allows the deep ocean to take up the excessive heat associated with sea-ice loss and reduces the spatial extent of the warming in the atmosphere. Thermal wind relation then translates the anomalous atmospheric warming structure into a latitudinal shift of the westerly jet.

Moreover, the fact that mixed-layer entrainment alone cannot efficiently remove the heat by horizontal transport highlights the function of AMOC: the AMOC removes the subsurface water carrying the heat entrained from the surface and replaces it with cold water. The uptake of thermal energy also dampens the ITCZ shift because it temporarily reduces the inter-hemispheric imbalance in the heat budget. Thus, entrainment affects the variability and large-scale energy transport when coupled with AMOC.

CTL_EMOM produces SST variability patterns that are in better agreement with those of the OGCM in the mid-latitude North Pacific, South Pacific, and North Atlantic oceans. Improvements in surface air temperature variability over North America and the Southern Ocean are likely associated with improved SST variability located upstream. In the sea-ice loss experiment, the Ekman flow amplifies the ITCZ shift, which contradicts past literature. This disagreement is due to the detail of Ekman parameterization, i.e., the inclusion of $\epsilon\tau^y$ and the choice of $H_{\mathrm{total}} = H_{\mathrm{EK}} + H_{\mathrm{RF}}$. Thus, the ITCZ response to sea-ice loss is sensitive to the Ekman parameterization.

In Section 2.6, we found a coupled positive feedback that originates from having insufficient diffusion to counteract the convergence of the frictional-Ekman flow. The feedback excites a coupled mode in which the convergence in the wind field enhances the convergence of warm surface water, that feeds back positively on the atmospheric convection and associated low-level convergence. This feedback generates erroneous rainband (Figure S1a) on the equator in the Central Pacific where the cold tongues are still poorly simulated in many climate models (Tian & Dong, 2020). It will be interesting in future studies to investigate whether this positive feedback and cold-tongue bias are connected.

Our hierarchy can still be refined depending on the need. For example:

- The nudging method used to derive the flux correction should account for the sea-ice concentration and thickness in addition to SST. Using information about the sea-ice field will resolve the fluxes of heat that are not accompanied by a change of temperature because of the phase change. In addition, diagnosing the interannual variability of sea-ice forming heat flux $\overline{\Lambda' T'}$ in Equation (11) from OGCM and subtracting it out of the flux correction may avoid double counting that causes the warm SST bias in the Southern Ocean along the sea-ice edges.
- The mixed-layer dynamics can further realize the K-profile parameterization (Large et al., 1994) or Niiler-Kraus type parameterization (Gaspar, 1988) so that it can respond dynamically to forcing. This improves the sub-seasonal to seasonal variability, which is important in the tropics.

Table 1. Sea-ice volume and area of CTL and SIL simulations in the northern and southern hemispheres.

	Sea-ice Volume [$\times 10^3\,\mathrm{km}^3$]				Sea-ice Area [$\times 10^6\,\mathrm{km}^2$]			
	NH		SH		NH		SH	
	CTL	SIL	CTL	SIL	CTL	SIL	CTL	SIL
OGCM	32.9	5.33	29.3	28.3	11.4	7.39	16.5	16.1
EMOM	26.2	5.20	21.0	19.5	10.8	7.02	14.4	13.7
MLM	26.5	5.21	23.6	23.1	10.8	7.02	15.1	14.9
SOM	28.7	5.25	30.4	30.1	11.3	7.15	16.9	16.8

- One can extend the current Ekman flow parameterization scheme by extending the thickness of the return flow layer H_{RF} from a constant to a spatially varying variable to account for sensitivity of $\mathrm{OHT}_{\mathrm{EK}}$ to H_{RF}. Devising a framework to diagnose H_{RF} from an OGCM will be necessary.
- Rayleigh friction is not the best parameterization to replace the momentum diffusion. One can improve the Ekman flow parameterization using the original diffusion form $\partial_z(K_{\mathrm{m}}\partial_z\vec{v})$. Using this form leads to solving a fourth-order ordinary differential equation for each water column.
- Ocean gyres are important for mid- to high-latitude OHT, but it is non-trivial to simulate them directly. Still, if the gyre velocity does not change significantly, prescribing the ocean flow can be a workaround to achieve responsive temperature and salt advection.

Appendix A Sea-ice forcing

We apply the forcing by constraining sea-ice thickness. The target sea-ice thickness in our sea-ice thickness experiment is derived from years 2081–2100 of an ensemble member of Rep-

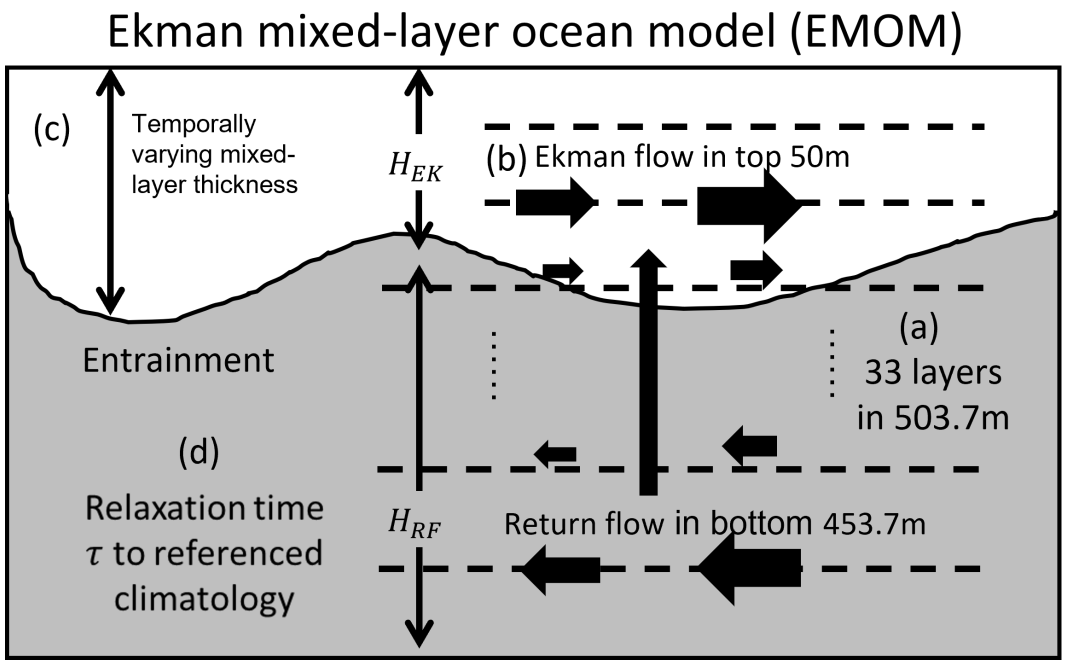

Figure 1. Schematic diagram of EMOM architecture. (a) EMOM has 33 vertical layers whose total depth is $\approx$ 503.7 m and range in thickness from 10 m to 48 m. (b) The Ekman and return flow layers have thicknesses of 50 m and 453.7 m. (c) EMOM has a time-varying mixed-layer thickness to capture the effect of seasonal entrainment and detrainment. (d) The ocean temperature and salinity are relaxed toward a reference three-dimensional profile with a 100-year timescale.

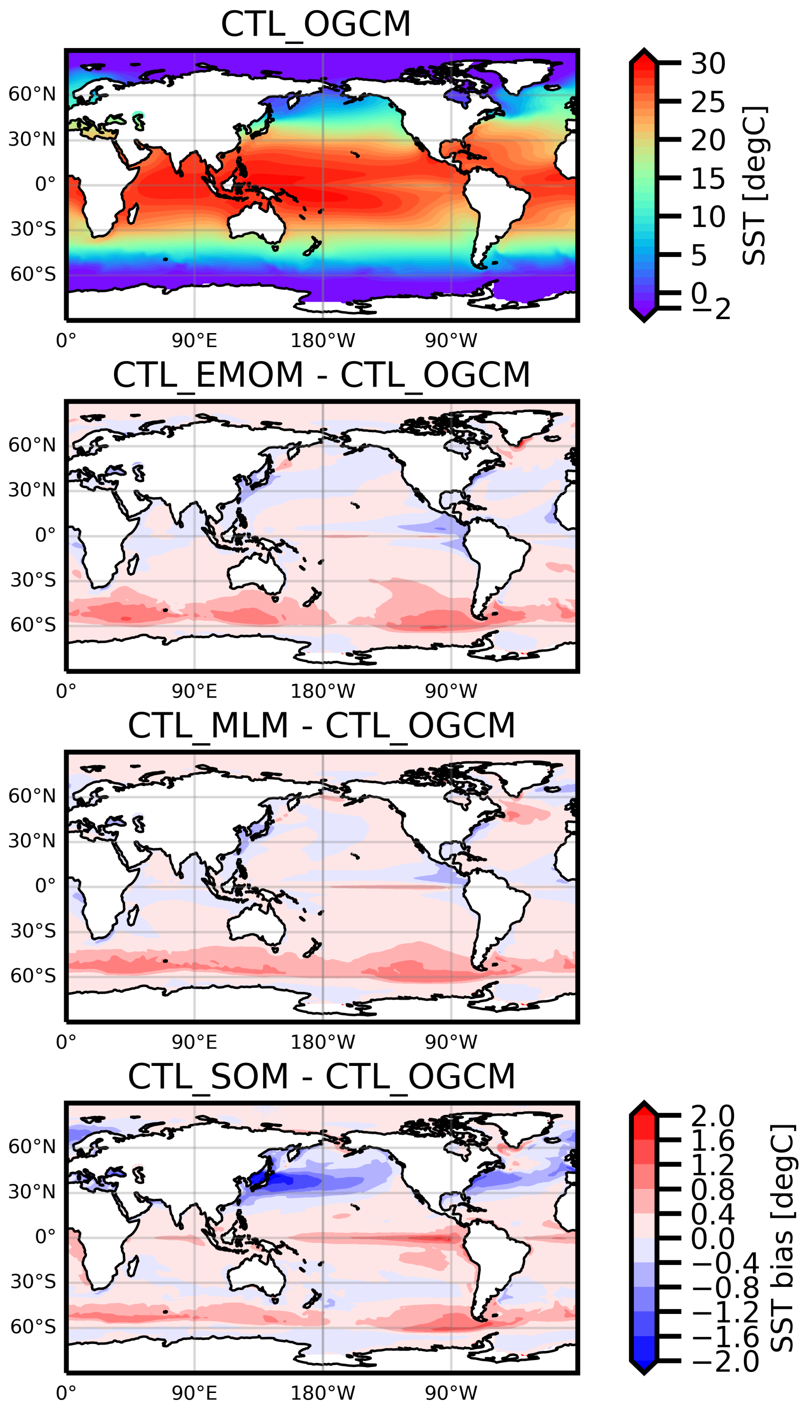

Figure 2. The annual mean SST of the hierarchy in CTL run. The top panel shows the target climatology obtained from the run using the full OGCM. The other panels show the biases in the other hierarchy members, i.e., (CTL_[member] - CTL_OGCM).

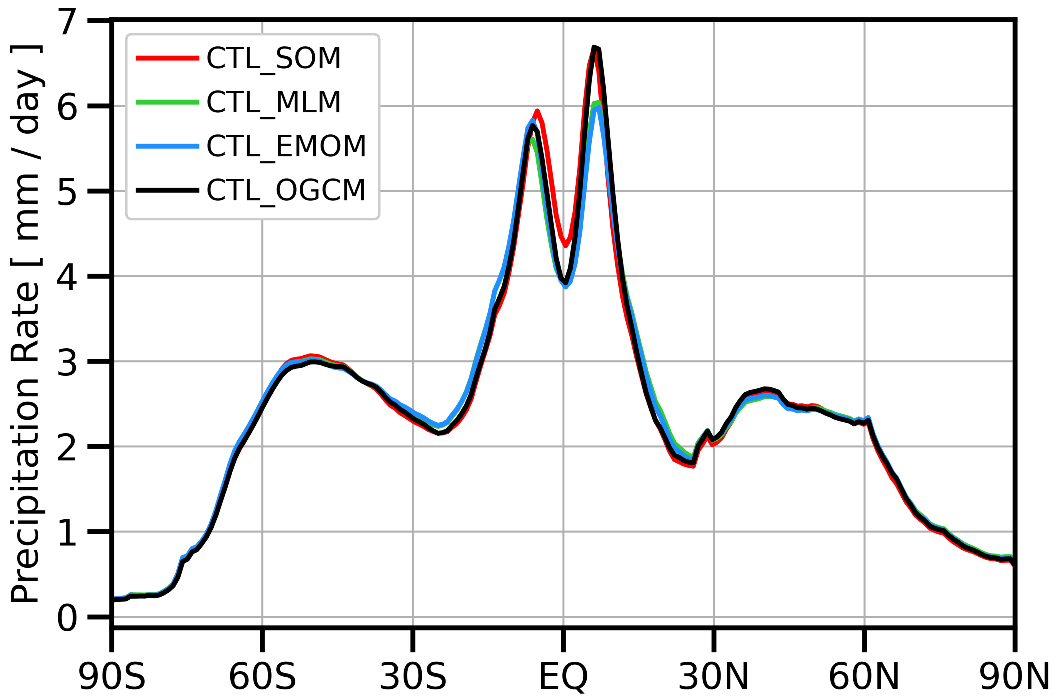

Figure 3. The zonal mean of the annually-averaged precipitation for the CTL run.

resentative Concentration Pathway 8.5 (RCP8.5) in Coupled Model Intercomparison Project Phase 5 (CMIP5) that is simulated using CCSM4. The total sea-ice volume in the SIL is about one-sixth of that in the CTL with an almost sea-ice-free Arctic in September. The distribution of mean sea-ice thickness is shown in Figure S3.

The target sea-ice thickness is achieved by imposing a pseudo heat flux to the sea-ice model,

$$F_{\text{pseudo}} = \frac{L_{\text{ice}}\rho_{\text{ice}}}{\tau_{\text{nudging}}}\left(h_{\text{model}} - h_{\text{target}}\right), \tag{A1}$$

where h_{model} and h_{target} are the sea-ice thicknesses of the current time step and the target, F_{pseudo} is the pseudo heat flux with the sign chosen so that $F_{\text{pseudo}} > 0$ indicates an energy flux into the sea ice, $L_{\text{ice}} = 3.34 \times 10^5\,\text{J}/\text{kg}$ the specific latent heat fusion for sea ice, $\rho_{\text{ice}} = 917\,\text{kg}/\text{m}^3$ the sea ice density, $\tau_{\text{nudging}} = 5$ days is the nudging timescale, and h_{model} and h_{target} are the modeled and target sea-ice thicknesses. If the modeled sea-ice thickness is larger than the target sea-ice thickness then a heat gain causes the ice volume to decrease. Conversely, if the modeled sea-ice thickness is less than the target sea-ice thickness then a heat loss causes the ice volume to increase

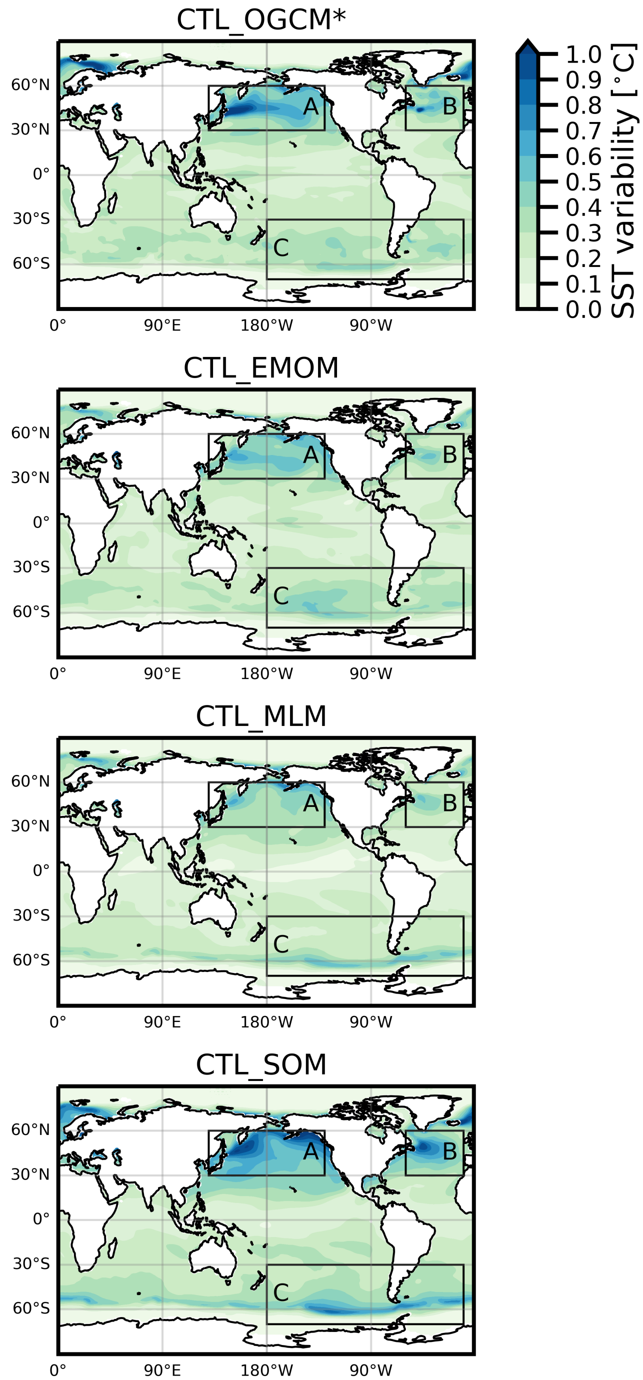

Figure 4. The annual mean SST variability (standard deviation of SSTA) of CTL run. The variability in CTL_OGCM* is computed by removing the anomalies that are correlated with the time series of the first empirical orthogonal function of monthly SSTA between 20°S–20°N. Boxes A, B, and C show the regions that have the biggest differences.

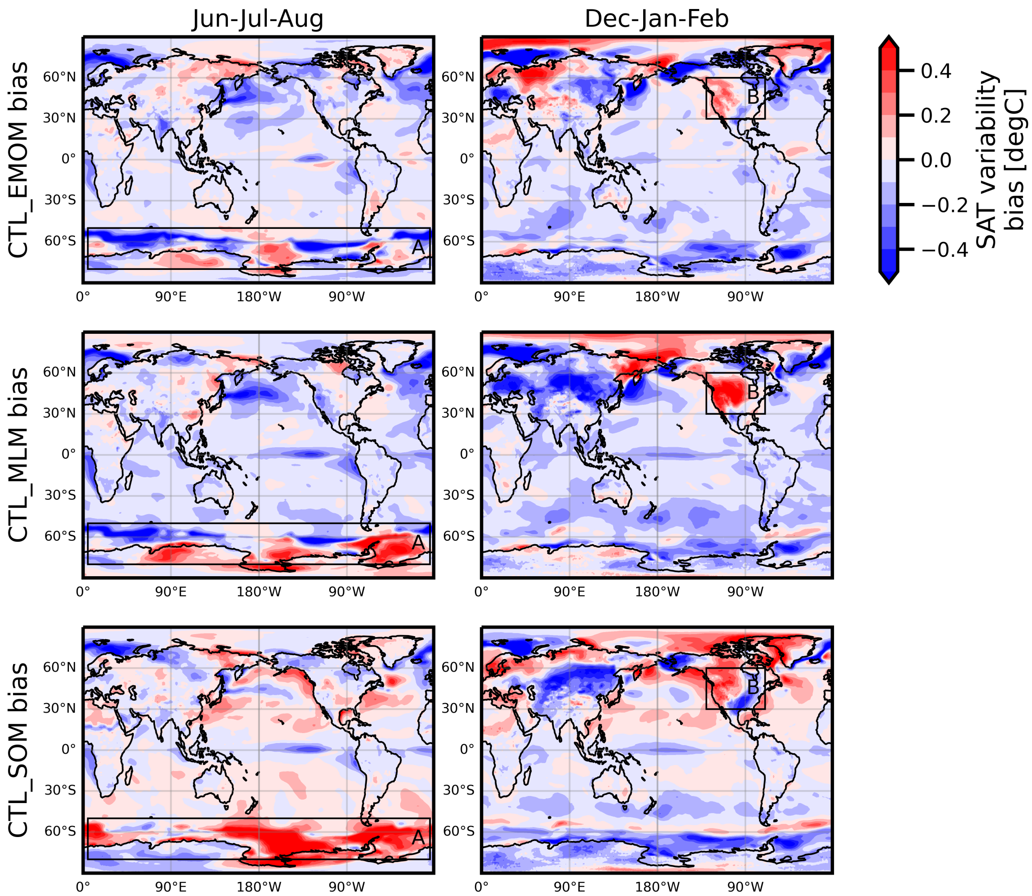

Figure 5. The Jun-Jul-Aug and Dec-Jan-Feb mean SAT variability bias (CTL_[member] - CTL_OGCM*). See the caption for Figure 4 for the definition of CTL_OGCM*. Boxes A, B, and C show regions of major SAT improvements that originate from the inclusion of Ekman flow.

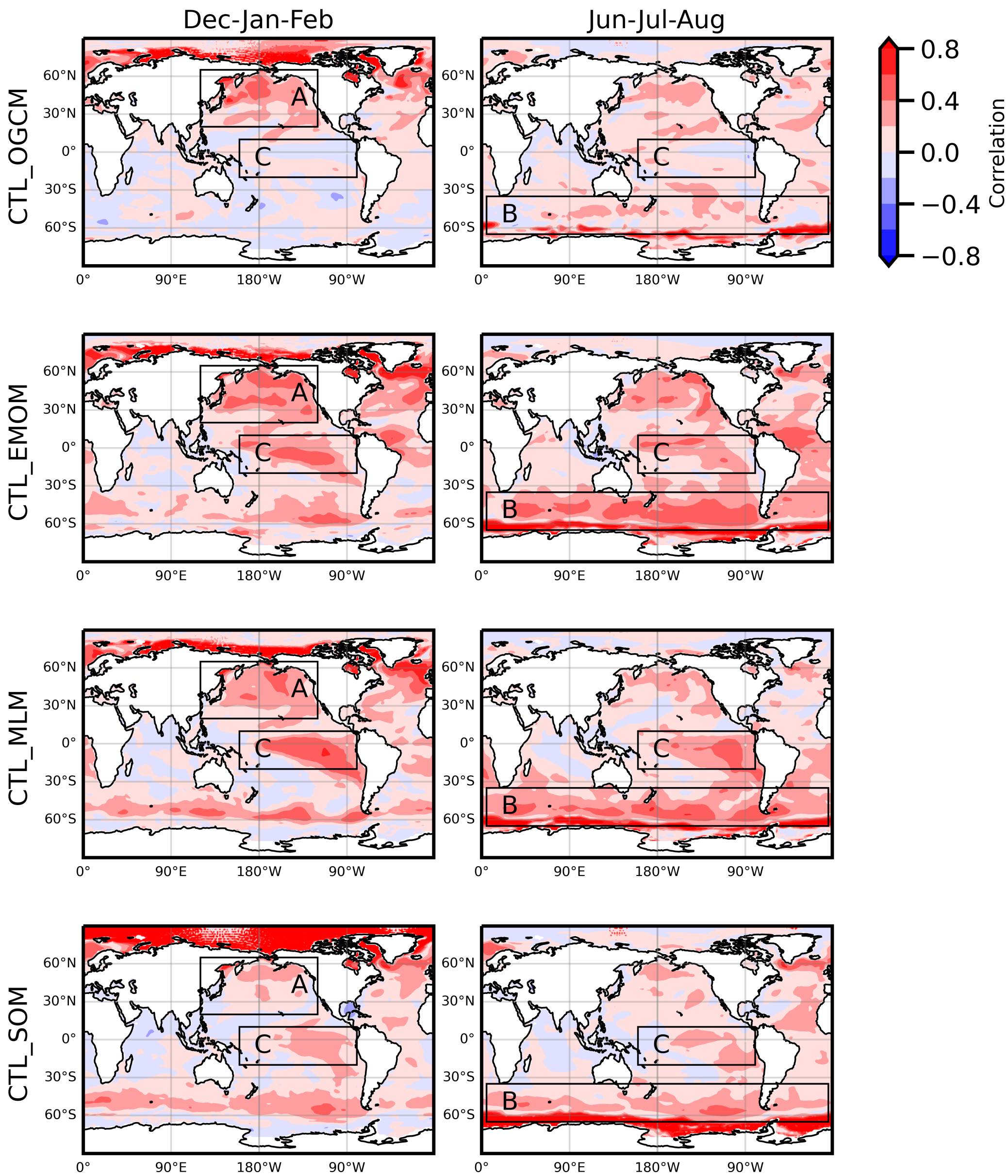

Figure 6. SSTA winter-to-winter correlation. Here Dec-Jan-Feb and Jun-Jul-Aug are winters in northern and southern hemispheres, respectively. Box A shows the improvement over the Northern Pacific as more ocean processes are included. Boxes B and C show that there are major processes not captured in simplified models that removes the memory. In box B, we speculate these are the northward transport of the subducted Antarctic Intermediate Water and the diffusive effect of eddies. In box C, horizontal currents and wave dynamics might act to dampen the SSTA efficiently.

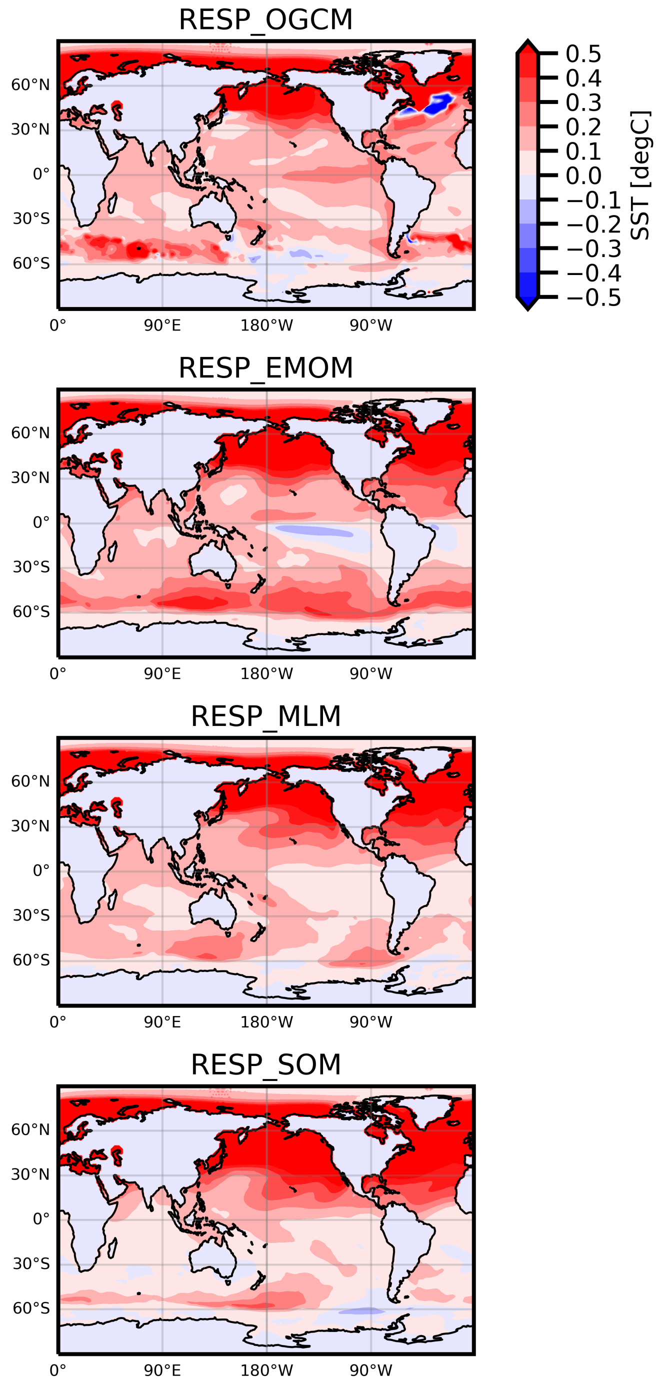

Figure 7. The annual mean SST response to Arctic sea-ice loss. The response is defined as RESP_[member] := SIL_[member] - CTL_[member]. As we move up the hierarchy, the extent of SST warming decreases, demonstrating the ocean's improved ability to buffer the effect of the warming as more processes are included.

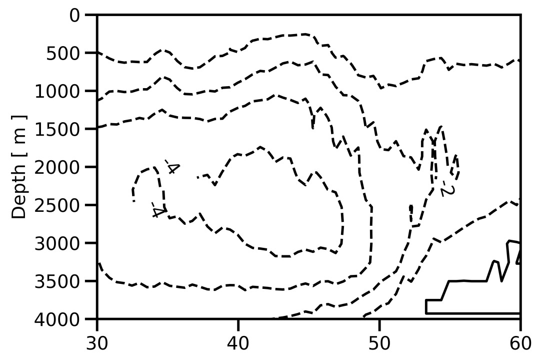

Figure 8. The AMOC streamfunction response to the loss of Arctic sea-ice. The contour spacing is 1 Sv = $1 \times 10^6\,\mathrm{m}^3/\mathrm{s}$. The anomalous upwelling that removes the entrained heat from the surface is located between 40°N-60°N. The heat removal creates the warming hole over the North Atlantic, as seen in Figure 7.

towards the target. The model we use divides the sea ice into five different categories with each having its own equivalent sea-ice thickness. Since we do not differentiate them, we use the value of their sum as sea-ice thickness in the equation above. Nudging the sea-ice thickness does not uniquely determine sea ice concentration which might give rise to inconsistent ice albedo and heat exchange if forcing is weak (Sun et al., 2020). Since our forcing is very strong the discrepancy is negligible.

Appendix B Temporally Varying Mixed-layer Depth Changes SST variability

We construct a one-dimensional mixed-layer model by vertically integrating Equation (1a) from the bottom of mixed-layer to the surface to get an approximated well-mixed mixed-layer model as

$$\frac{\partial T_{\mathrm{mix}}}{\partial t} = -\frac{F_{\mathrm{net}}}{\rho c_p h} - \frac{w_e}{h}\left(T_{\mathrm{mix}} - T_d\right) + q$$

where T_{mix} is the mixed-layer ocean temperature, $F_{\mathrm{net}} = F(z=0) - F(z=-h)$ is the net incoming energy flux into the mixed-layer, T_d is the temperature immediately below the mixed-layer, $w_e = \max(\partial h/\partial t, 0)$ is the entrainment velocity, and q is the sum of freezing and advection tendency terms. Taking the deviation (denoted with a prime) from the seasonal mean (denoted with

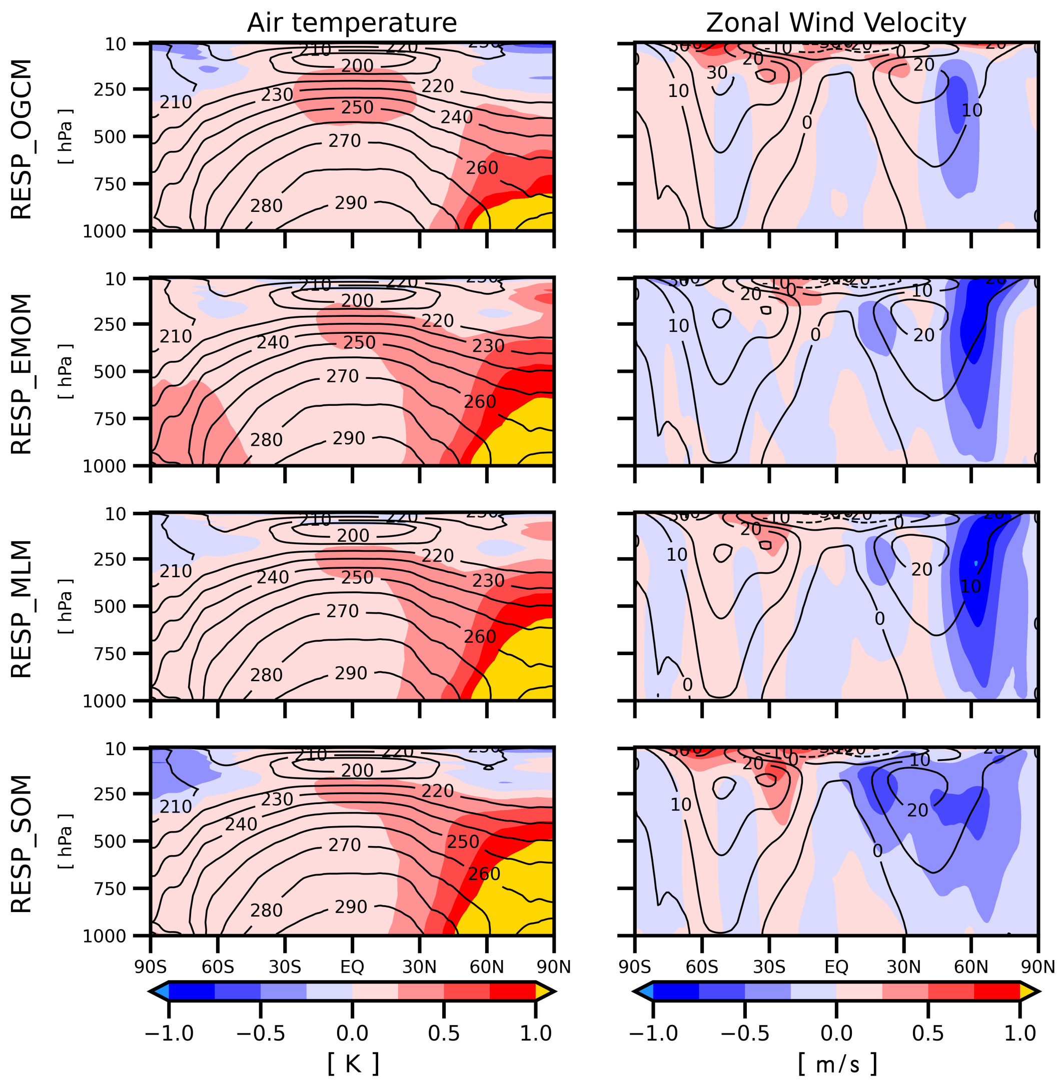

Figure 9. The zonal mean response of the atmosphere to Arctic sea-ice loss. The shading shows the response (RESP_[member] := SIL_[member] - CTL_[member]) of zonal mean air temperature (left column) and zonally mean zonal wind (right column). The contours show the quantities in CTL_[member].

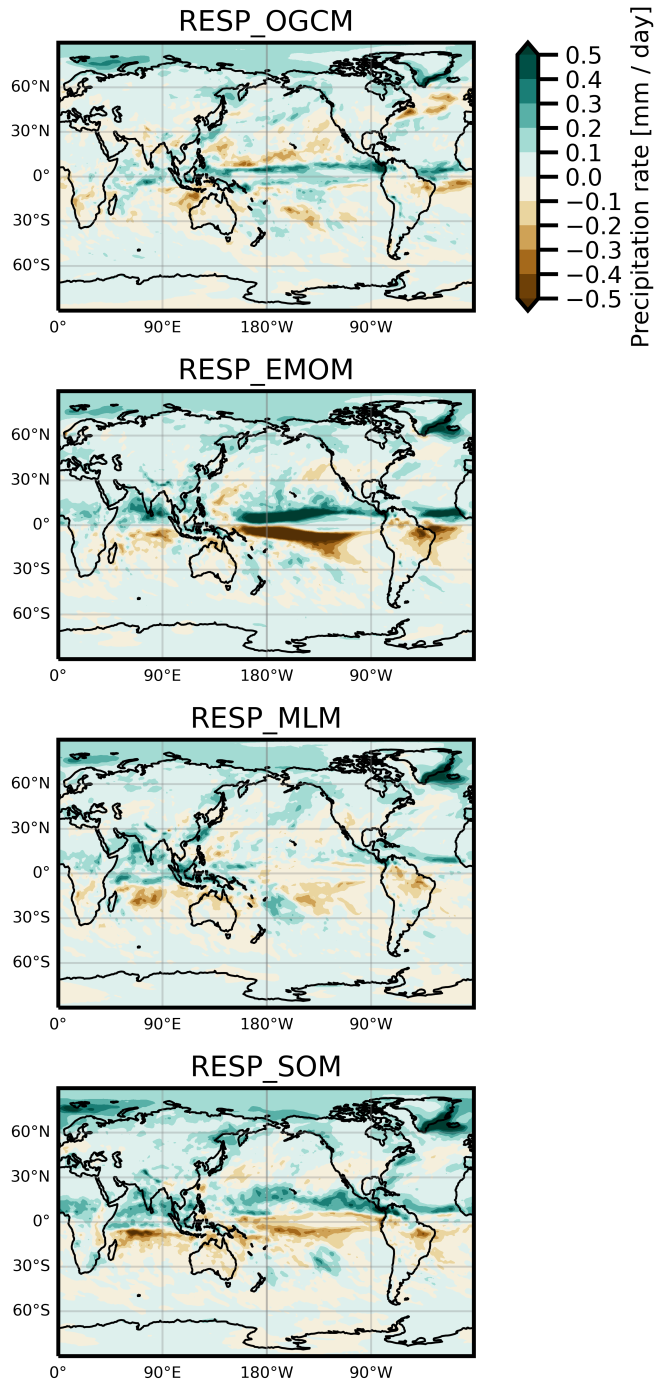

Figure 10. Similar to Figure 7 but for annual mean precipitation. Most of the responses locate in the tropics. RESP_OGCM shows a narrowing of ITCZ in the Pacific but a northward shift in the Atlantic. Rest of the models show various degree of northward shift of ITCZ.

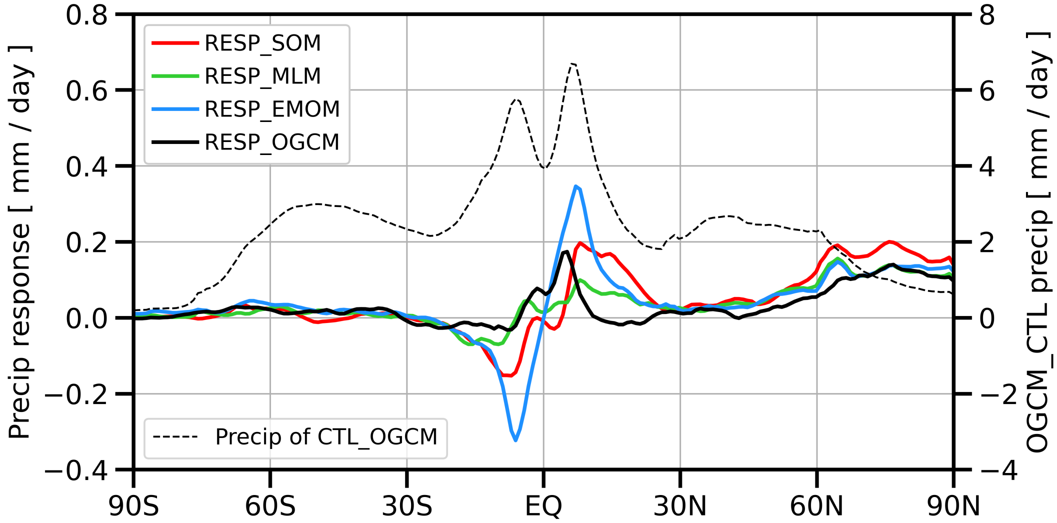

Figure 11. Response of zonal mean of annual precipitation (RESP_[member] := SIL_[member] - CTL_[member]; left ticks). Dashed line shows the precipitation in CTL_OGCM (right ticks).

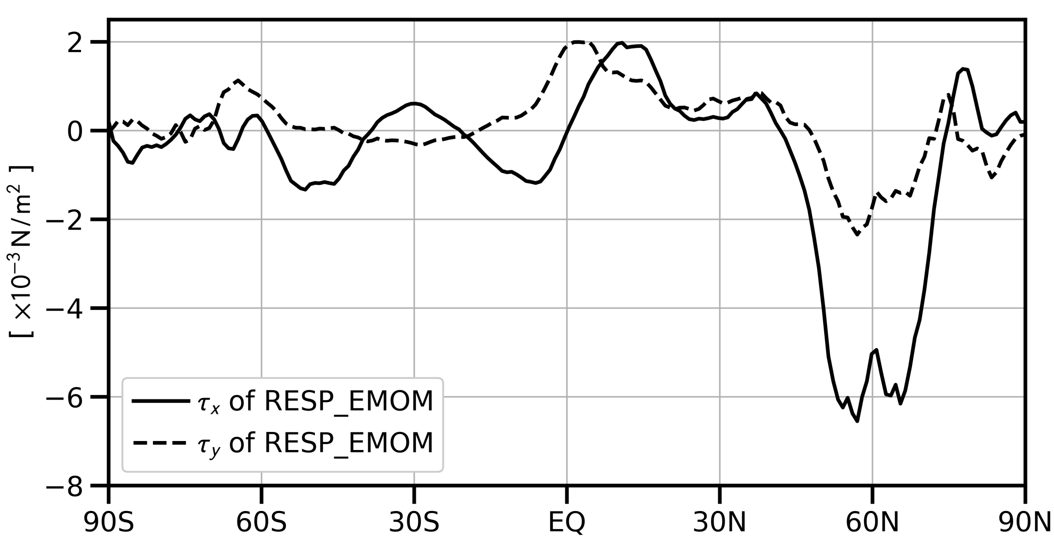

Figure 12. The response of surface zonal wind stress τ_x (solid; positive values means eastward wind anomalies) and meridional wind stress (dashed; positive values means northward wind anomalies) in EMOM.

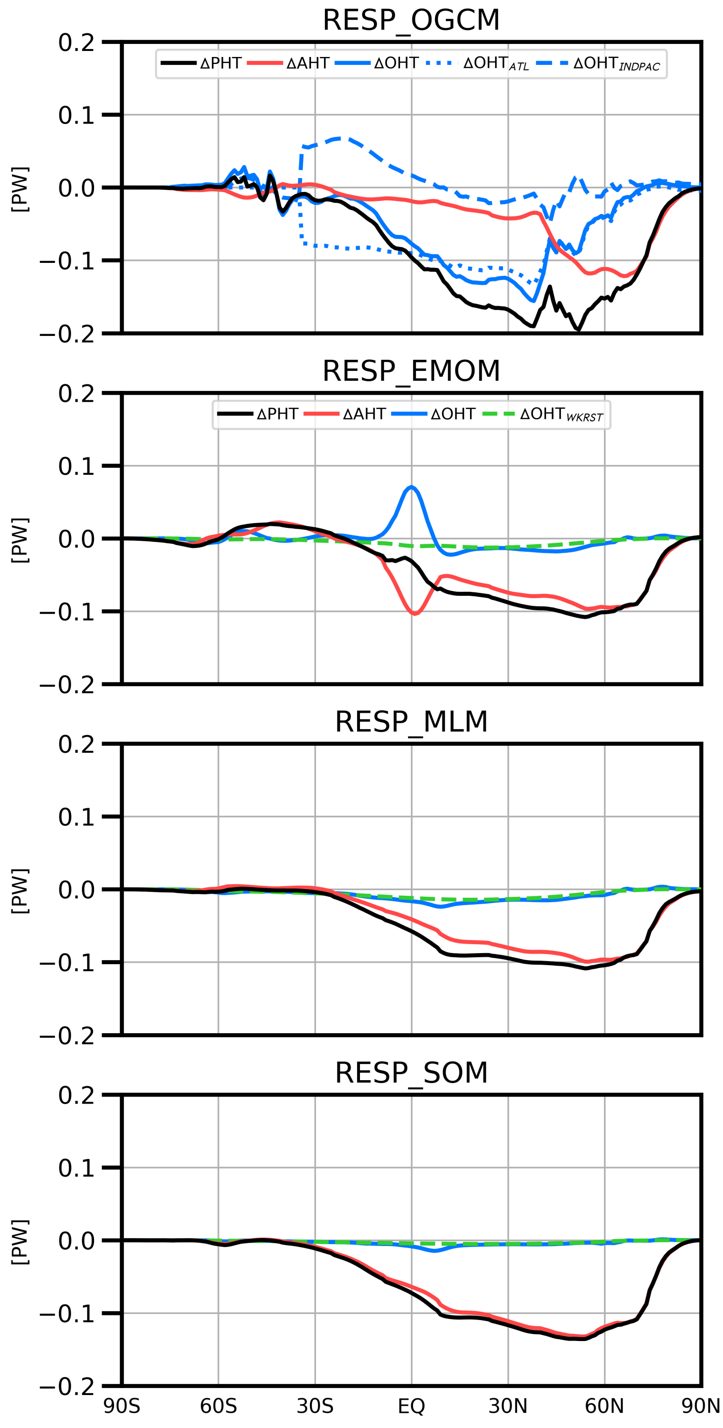

Figure 13. Heat transport response analysis. PHT = AHT + OHT. The OHT in RESP_OGCM is further decomposed into Indian-Pacific and Atlantic basins (ΔOHT_{INDPAC} and ΔOHT_{ATL}). In the simplified models, we also plot out the OHT due to weak-restoring (ΔOHT_{WKRST}) to show it is a minor component. In RESP_SOM and RESP_MLM, OHT is fully contributed by diffusion.

an overbar) we get

$$\frac{\partial T'_{\text{mix}}}{\partial t} \approx -\frac{F'_{\text{net}}}{\rho c_p \overline{h}} + \frac{\overline{F}_{\text{net}}}{\rho c_p \overline{h}^2} h' - \left(\frac{w_e}{h}\right)' \left(\overline{T}_{\text{mix}} - \overline{T}_d\right) - \frac{\overline{w}_e}{\overline{h}} \left(T'_{\text{mix}} - T'_d\right) + q' - \frac{1}{\tau_{\text{adj}}} T'$$

$$= -\frac{F'_{\text{net}}}{\rho c_p \overline{h}} - \frac{\overline{w}_e}{\overline{h}} T' - \frac{1}{\tau_{\text{adj}}} T' \tag{B1}$$

where the last term on the right-hand side is the damping of temperature anomaly due to air-sea interaction with time scale τ_{adj}. We drop the deviation terms related to h because we prescribed its annual evolution; we also drop q' because in the MLM model there is no advection and most of the ocean is sea-ice free; furthermore, we drop T_d for it is expected that $|T'_d| \ll |T'|$. We hypothesize that it is the existence of entrainment that reduces the SSTA variance.

Since strictly speaking, $\overline{h}$ used in SOM is the temporal mean of $\overline{h}$ in MLM so the first term on the right-hand side is also different, we should support this hypothesis by conducting stochastic simulations of Equation (B1).

We set

$$\overline{h}(t) = h_{\text{m}} + \frac{h_{\text{amp}}}{2} \sin\left(\frac{2\pi}{P} t\right) \tag{B2}$$

$$F'_{\text{net}}(t) = \left[F_{\text{m}} + \frac{F_{\text{amp}}}{2} \sin\left(\frac{2\pi}{P} t\right)\right] \epsilon'(t) \tag{B3}$$

where $P = 360$ days is the annual cycle period, $h_{\text{m}} = 70$ m is the mean mixed-layer thickness, h_{amp} is the amplitude of mixed-layer variation, $F_{\text{m}} = 30\,\text{W/m}^2$ and F_{amp} are the same but for F'_{net}, $\epsilon' \sim N$ is a Gaussian noise. It is designed so such that the thicker mixed-layer thickness coincide with higher surface energy flux variance as observed in coupled simulations. SOM is represented by setting $h_{\text{amp}} = 0$ m and MLM by $h_{\text{amp}} = 60$ m. In all numerical integration we select $\tau_{\text{adj}} = 180$ days, $T'_{\text{mix}}(t = 0) = 0$, and Euler forward scheme with time step 30 days is used. For each simulation, integrate for 100-thousand years and compute the resulting monthly mean values (30 days per month), then use the resulting T'_{mix} time series to compute one standard deviation value.

Assigning $F_{\text{amp}} = 0\,\text{W/m}^2$, the SST variability of SOM and MLM are 0.27°C and 0.21°C. Further assigning $F_{\text{amp}} = 40\,\text{W/m}^2$ we get 0.30°C and 0.20°C. The even larger separation is because larger atmospheric stochastic forcing (winter) is efficiently damped by thicker mixed-layer depth. These two sets experiments show that the main cause of lower SST variability in MLM comes from the temporally varying mixed-layer depth.

Open Research

The simulation output data is available upon request. Please contact the authors through the email address provided.

Acknowledgments

This work is supported by the Department of Energy Grant DE-SC0019407. Computational resources were also provided by National Center for Atmospheric Research supercomputer Cheyenne.

References

Adam, O. (2021). Dynamic and energetic constraints on the modality and position of the intertropical convergence zone in an aquaplanet. *Journal of Climate*, *34*(2), 527–543.

Afargan-Gerstman, H., & Adam, O. (2020). Nonlinear damping of itcz migrations due to ekman ocean energy transport. *Geophysical Research Letters*, *47*(5), e2019GL086445.

Alexander, M. A., & Deser, C. (1995). A mechanism for the recurrence of wintertime midlatitude sst anomalies. *Journal of physical oceanography*, *25*(1), 122–137.

Alexander, M. A., Deser, C., & Timlin, M. S. (1999). The reemergence of sst anomalies in the north pacific ocean. *Journal of climate*, *12*(8), 2419–2433.

Alexander, M. A., & Scott, J. D. (2008). The role of ekman ocean heat transport in the northern hemisphere response to enso. *Journal of climate*, *21*(21), 5688–5707.

Alexander, M. A., Scott, J. D., & Deser, C. (2000). Processes that influence sea surface temperature and ocean mixed layer depth variability in a coupled model. *Journal of Geophysical Research: Oceans*, *105*(C7), 16823–16842.

Bitz, C. M., Shell, K., Gent, P., Bailey, D., Danabasoglu, G., Armour, K., . . . Kiehl, J. (2012). Climate sensitivity of the community climate system model, version 4. *Journal of Climate*, *25*(9), 3053–3070.

Bryan, K., & Cox, M. D. (1972). An approximate equation of state for numerical models of ocean circulation. *J. Phys. Oceanogr*, *2*(4), 510–514.

Claussen, M., Mysak, L., Weaver, A., Crucifix, M., Fichefet, T., Loutre, M.-F., ... others (2002). Earth system models of intermediate complexity: closing the gap in the spectrum of climate system models. *Climate dynamics*, *18*(7), 579–586.

Codron, F. (2012). Ekman heat transport for slab oceans. *Climate Dynamics*, *38*(1-2), 379–389.

Danabasoglu, G., Bates, S. C., Briegleb, B. P., Jayne, S. R., Jochum, M., Large, W. G., ... Yeager, S. G. (2012). The ccsm4 ocean component. *Journal of Climate*, *25*(5), 1361–1389.

Donohoe, A., Frierson, D. M., & Battisti, D. S. (2014). The effect of ocean mixed layer depth on climate in slab ocean aquaplanet experiments. *Climate dynamics*, *43*(3-4), 1041–1055.

Gaspar, P. (1988). Modeling the seasonal cycle of the upper ocean. *Journal of Physical Oceanography*, *18*(2), 161–180.

Gent, P. R., Danabasoglu, G., Donner, L. J., Holland, M. M., Hunke, E. C., Jayne, S. R., ... others (2011). The community climate system model version 4. *Journal of climate*, *24*(19), 4973–4991.

Gent, P. R., & McWilliams, J. C. (1990). Isopycnal mixing in ocean circulation models. *Journal of Physical Oceanography*, *20*(1), 150–155.

Green, B., & Marshall, J. (2017). Coupling of trade winds with ocean circulation damps itcz shifts. *Journal of Climate*, *30*(12), 4395–4411.

Green, B., Marshall, J., & Campin, J.-M. (2019). The ‘sticky’itcz: ocean-moderated itcz shifts. *Climate dynamics*, *53*(1-2), 1–19.

Haarsma, R. J., Campos, E. J., Hazeleger, W., Severijns, C., Piola, A. R., & Molteni, F. (2005). Dominant modes of variability in the south atlantic: A study with a hierarchy of ocean–atmosphere models. *Journal of climate*, *18*(11), 1719–1735.

Held, I. M. (2001). The partitioning of the poleward energy transport between the tropical ocean and atmosphere. *Journal of the atmospheric sciences*, *58*(8), 943–948.

Held, I. M. (2005). The gap between simulation and understanding in climate modeling. *Bulletin of the American Meteorological Society*, *86*(11), 1609–1614.

Hirons, L., Klingaman, N., & Woolnough, S. (2015). Metum-goml: a near-globally coupled atmosphere–ocean-mixed-layer model. *Geoscientific Model Development*, *8*, 363–379.

Hunke, E. C., Lipscomb, W. H., Turner, A. K., Jeffery, N., & Elliott, S. (2010). Cice: the los alamos sea ice model documentation and software user's manual version 4.1 la-cc-06-012. *T-3 Fluid Dynamics Group, Los Alamos National Laboratory*, *675*, 500.

Hurrell, J. W., Holland, M. M., Gent, P. R., Ghan, S., Kay, J. E., Kushner, P. J., . . . others (2013). The community earth system model: a framework for collaborative research. *Bulletin of the American Meteorological Society*, *94*(9), 1339–1360.

Jayne, S. R., & Marotzke, J. (2001). The dynamics of ocean heat transport variability. *Reviews of Geophysics*, *39*(3), 385–411.

Jeevanjee, N., Hassanzadeh, P., Hill, S., & Sheshadri, A. (2017). A perspective on climate model hierarchies. *Journal of Advances in Modeling Earth Systems*, *9*(4), 1760–1771.

Kang, S. M. (2020). Extratropical influence on the tropical rainfall distribution. *Current Climate Change Reports*, *6*(1), 24–36.

Kang, S. M., Shin, Y., & Codron, F. (2018). The partitioning of poleward energy transport response between the atmosphere and ekman flux to prescribed surface forcing in a simplified gcm. *Geoscience Letters*, *5*(1), 22.

Kang, S. M., Shin, Y., & Xie, S.-P. (2018). Extratropical forcing and tropical rainfall distribution: energetics framework and ocean ekman advection. *npj Climate and Atmospheric Science*, *1*(1), 1–10.

Kiehl, J. T., Shields, C. A., Hack, J. J., & Collins, W. D. (2006). The climate sensitivity of the community climate system model version 3 (ccsm3). *Journal of Climate*, *19*(11), 2584–2596.

Kwon, Y.-O., Deser, C., & Cassou, C. (2011). Coupled atmosphere–mixed layer ocean response to ocean heat flux convergence along the kuroshio current extension. *Climate* *dynamics*, *36*(11-12), 2295–2312.

Large, W. G., McWilliams, J. C., & Doney, S. C. (1994). Oceanic vertical mixing: A review and a model with a nonlocal boundary layer parameterization. *Reviews of Geophysics*, *32*(4), 363–403.

Lawrence, D. M., Oleson, K. W., Flanner, M. G., Thornton, P. E., Swenson, S. C., Lawrence, P. J., . . . others (2011). Parameterization improvements and functional and structural advances in version 4 of the community land model. *Journal of Advances in Modeling Earth Systems*, *3*(1).

Lee, T., & Marotzke, J. (1998). Seasonal cycles of meridional overturning and heat transport of the indian ocean. *Journal of Physical Oceanography*, *28*(5), 923–943.

Leonard, B. P. (1979). A stable and accurate convective modelling procedure based on quadratic upstream interpolation. *Computer methods in applied mechanics and engineering*, *19*(1), 59–98.

Maher, P., Gerber, E. P., Medeiros, B., Merlis, T. M., Sherwood, S., Sheshadri, A., . . . Zurita-Gotor, P. (2019). Model hierarchies for understanding atmospheric circulation. *Reviews of Geophysics*, *57*(2), 250–280.

Neale, R. B., Richter, J., Park, S., Lauritzen, P. H., Vavrus, S. J., Rasch, P. J., & Zhang, M. (2013). The mean climate of the community atmosphere model (cam4) in forced sst and fully coupled experiments. *Journal of Climate*, *26*(14), 5150–5168.

Newman, M., Alexander, M. A., Ault, T. R., Cobb, K. M., Deser, C., Di Lorenzo, E., . . . others (2016). The pacific decadal oscillation, revisited. *Journal of Climate*, *29*(12), 4399–4427.

Niiler, P. (1977). One-dimensional models of the upper ocean. modelling and prediction of the upper layers of the ocean, eb kraus, ed. *Pergamon Press*, *143*, 172.

Nummelin, A., Busecke, J. J., Haine, T. W., & Abernathey, R. P. (2021). Diagnosing the scale-and space-dependent horizontal eddy diffusivity at the global surface ocean. *Journal of Physical Oceanography*, *51*(2), 279–297.

Paulson, C. A., & Simpson, J. J. (1977). Irradiance measurements in the upper ocean. *Jour-*

nal of Physical Oceanography, *7*(6), 952–956.

Schneider, T. (2017). Feedback of atmosphere-ocean coupling on shifts of the intertropical convergence zone. *Geophysical Research Letters*, *44*(22), 11–644.

Schneider, T., Bischoff, T., & Haug, G. H. (2014). Migrations and dynamics of the intertropical convergence zone. *Nature*, *513*(7516), 45–53.

Screen, J. A., Deser, C., Smith, D. M., Zhang, X., Blackport, R., Kushner, P. J., ... Sun, L. (2018). Consistency and discrepancy in the atmospheric response to arctic sea-ice loss across climate models. *Nature Geoscience*, *11*(3), 155.

Smith, D. M., Eade, R., M., A., H., A., A., C., S., C., ... others, W. A. (2022). Robust but weak winter atmospheric circulation response to future arctic sea ice loss. , acceptedthe double-itcz bias in cmip3, cmip5, and cmip6 models based on annual mean precipitation. *Nature Communications*.

Smith, R., Jones, P., Briegleb, B., Bryan, F., Danabasoglu, G., Dennis, J., ... others (2010). The parallel ocean program (pop) reference manual: ocean component of the community climate system model (ccsm) and community earth system model (cesm). *LAUR-01853*, *141*, 1–140.

Sun, L., Deser, C., Tomas, R. A., & Alexander, M. (2020). Global coupled climate response to polar sea ice loss: Evaluating the effectiveness of different ice-constraining approaches. *Geophysical Research Letters*, *47*(3), e2019GL085788.

Tian, B., & Dong, X. (2020). The double-itcz bias in cmip3, cmip5, and cmip6 models based on annual mean precipitation. *Geophysical Research Letters*, *47*(8), e2020GL087232.

Tomas, R. A., Deser, C., & Sun, L. (2016). The role of ocean heat transport in the global climate response to projected arctic sea ice loss. *Journal of Climate*, *29*(19), 6841–6859.

Vallis, G. K., Colyer, G., Geen, R., Gerber, E., Jucker, M., Maher, P., ... Thomson, S. I. (2018). Isca, v1. 0: A framework for the global modelling of the atmospheres of earth and other planets at varying levels of complexity. *Geoscientific Model Development*, *11*(3), 843–859.

Wang, Z., Schneider, E. K., & Burls, N. J. (2019). The sensitivity of climatological sst to slab ocean model thickness. *Climate Dynamics*, *53*(9), 5709–5723.

Figure 1.

Ekman mixed-layer ocean model (EMOM)

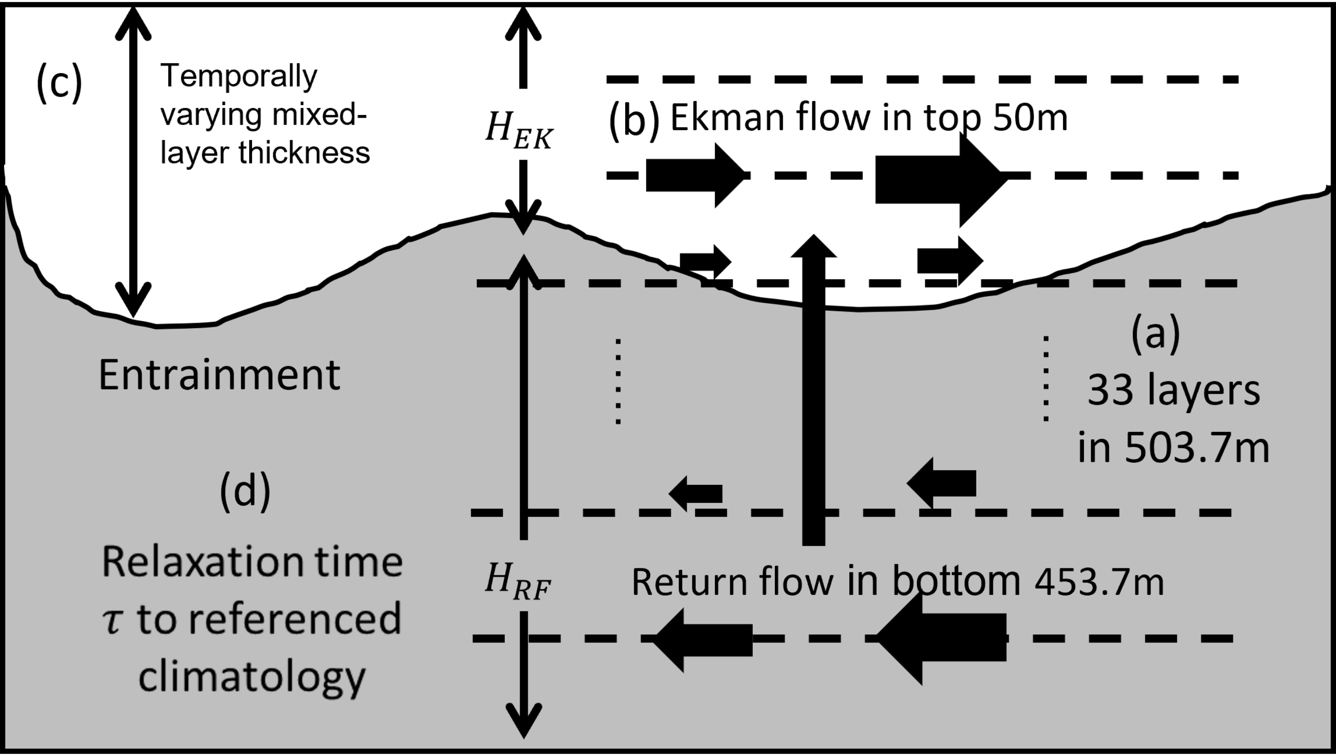

Figure 2.

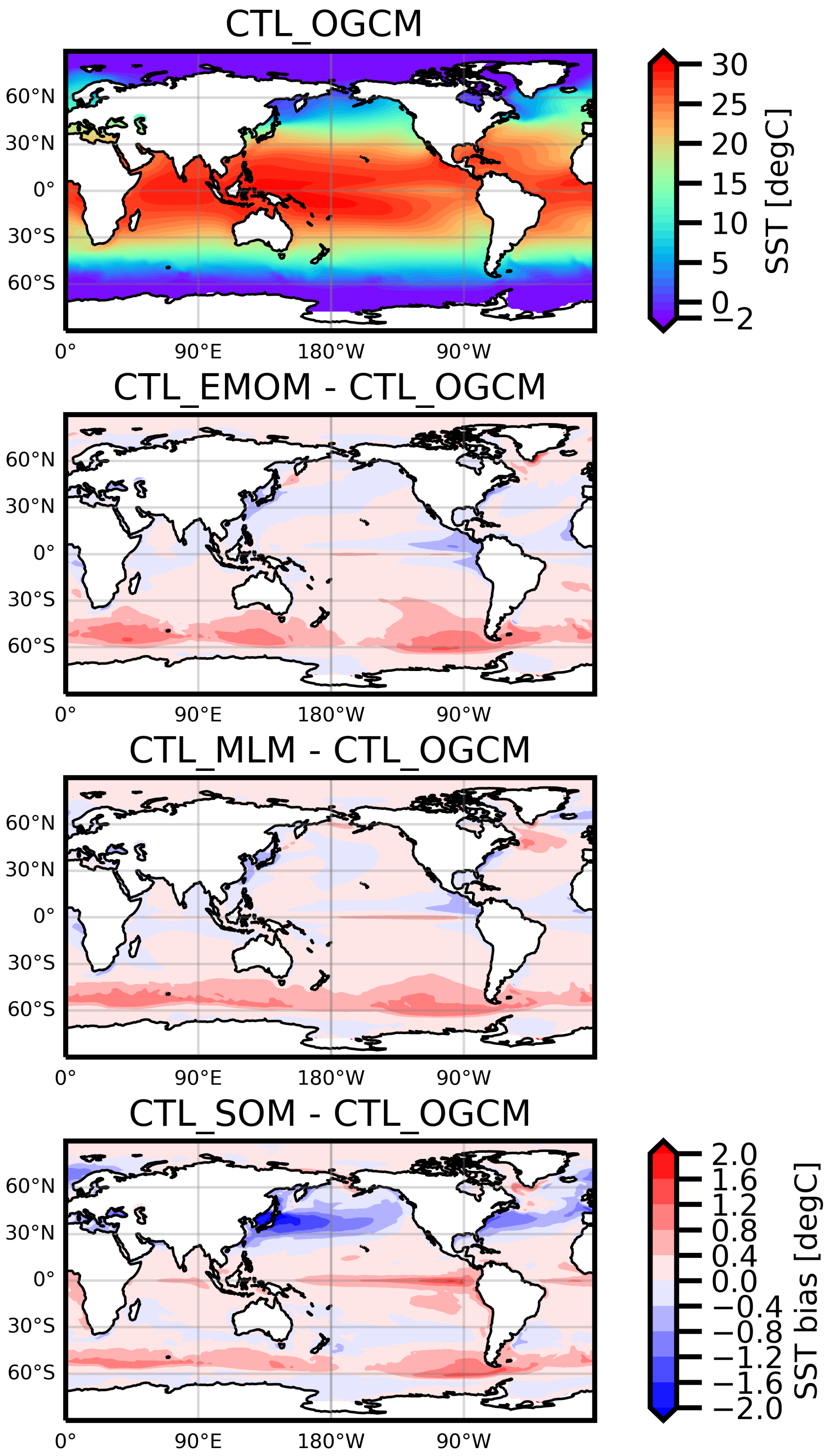
CTL_OGCM
CTL_EMOM - CTL_OGCM
CTL_MLM - CTL_OGCM
CTL_SOM - CTL_OGCM
60°N
30°N
0°
30°S
60°S
0°
90°E
180°W
90°W
SST [degC]
30
25
20
15
10
5
0
−2
SST bias [degC]
2.0
1.6
1.2
0.8
0.4
0.0
−0.4
−0.8
−1.2
−1.6
−2.0

Figure 3.

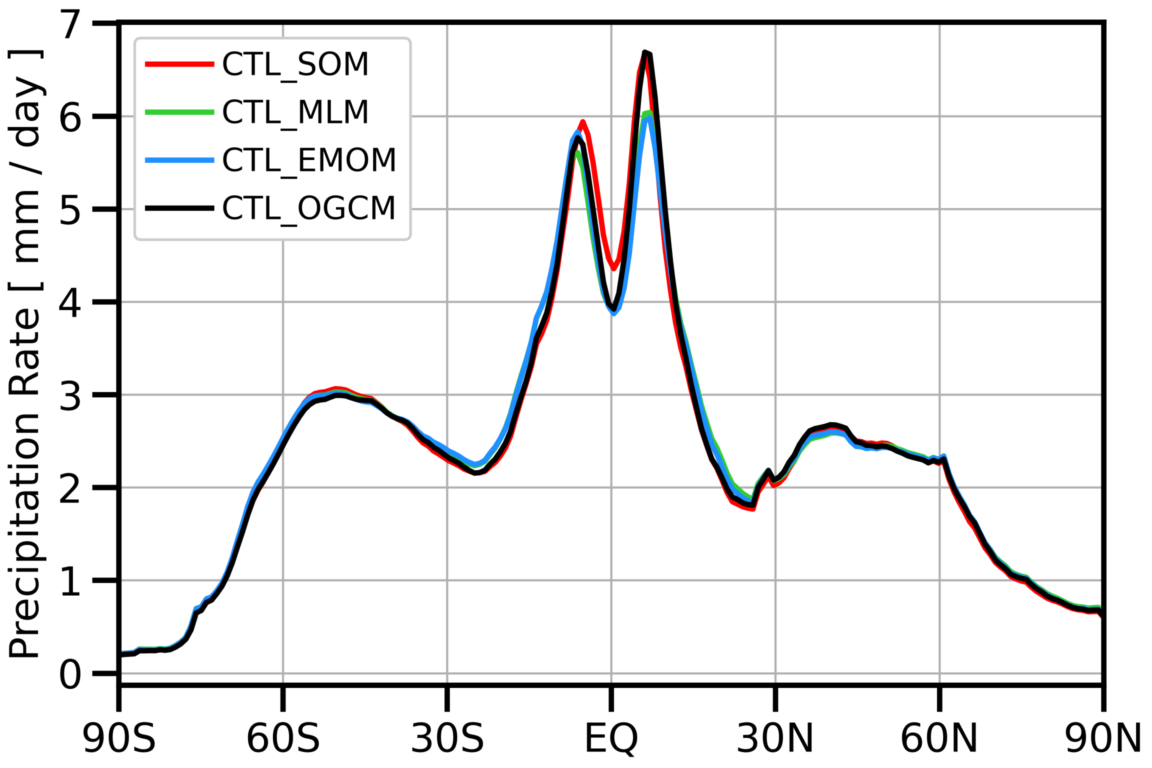

CTL_SOM
CTL_MLM
CTL_EMOM
CTL_OGCM
Precipitation Rate [mm / day]
0
1
2
3
4
5
6
7
90S
60S
30S
EQ
30N
60N
90N

Figure 4.

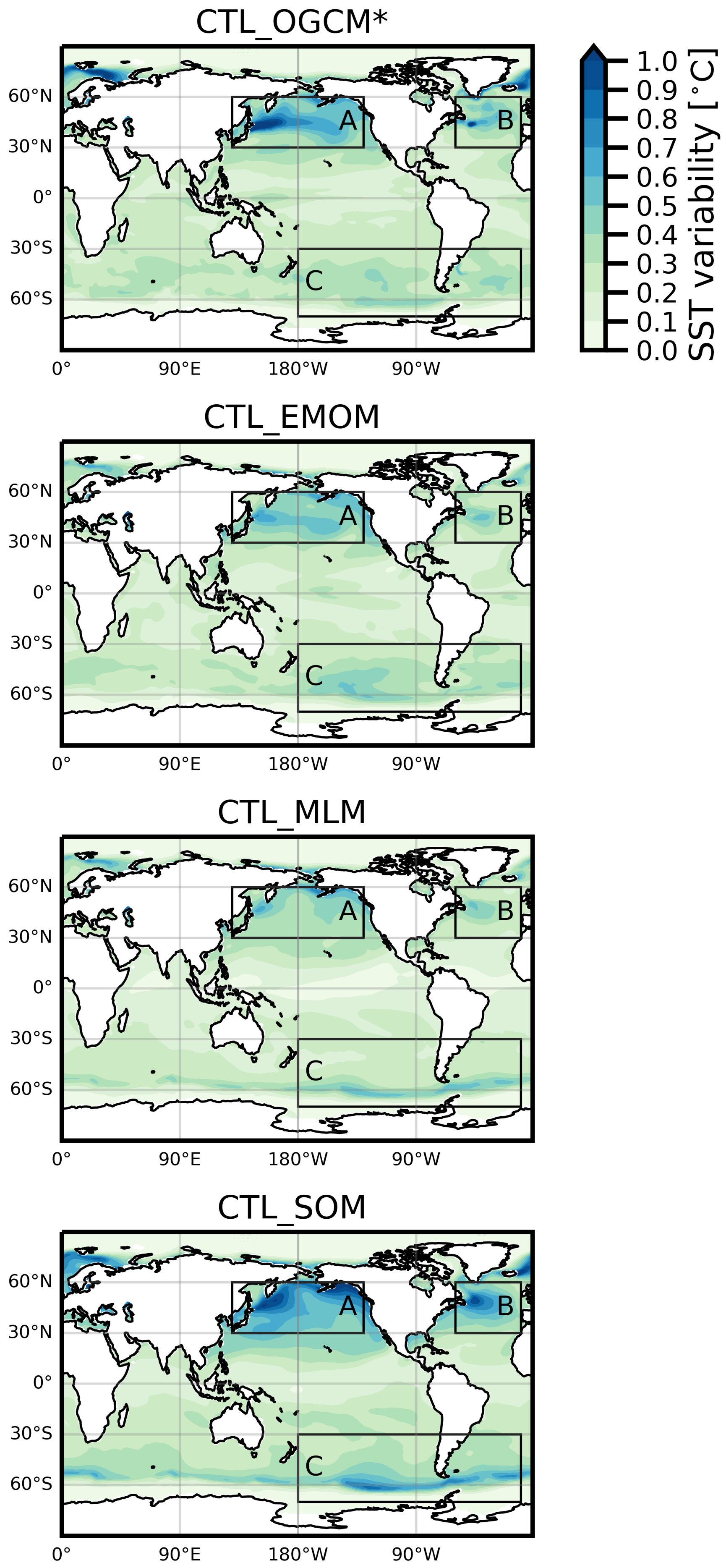

CTL_OGCM*
CTL_EMOM
CTL_MLM
CTL_SOM
A
B
C
60°N
30°N
0°
30°S
60°S
0°
90°E
180°W
90°W
SST variability [°C]
0.0
0.1
0.2
0.3
0.4
0.5
0.6
0.7
0.8
0.9
1.0

Figure 5.

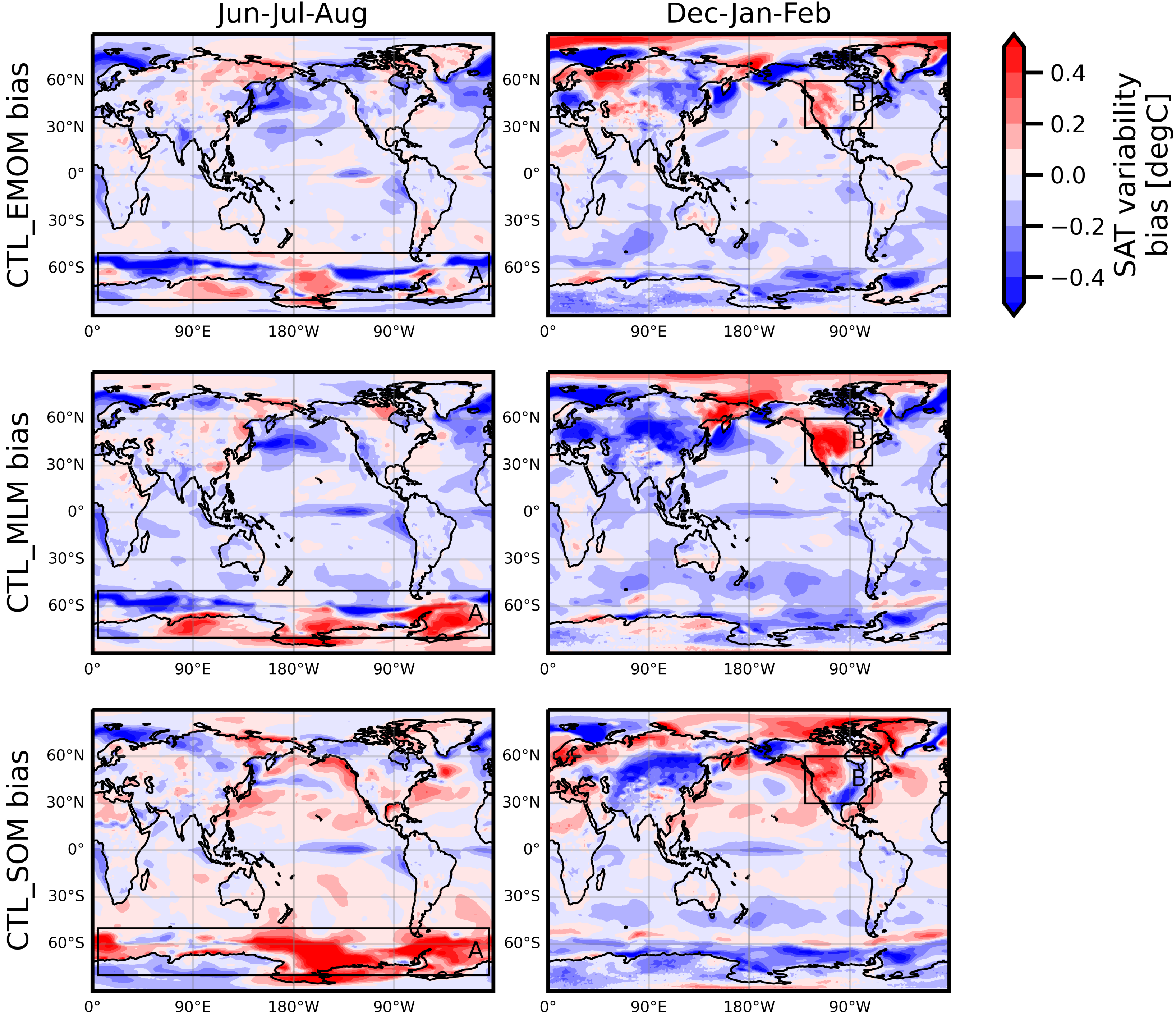

Jun-Jul-Aug
Dec-Jan-Feb
CTL_EMOM bias
CTL_MLM bias
CTL_SOM bias
SAT variability bias [degC]
0.4
0.2
0.0
−0.2
−0.4
60°N
30°N
0°
30°S
60°S
90°E
180°W
90°W
A
B

Figure 6.

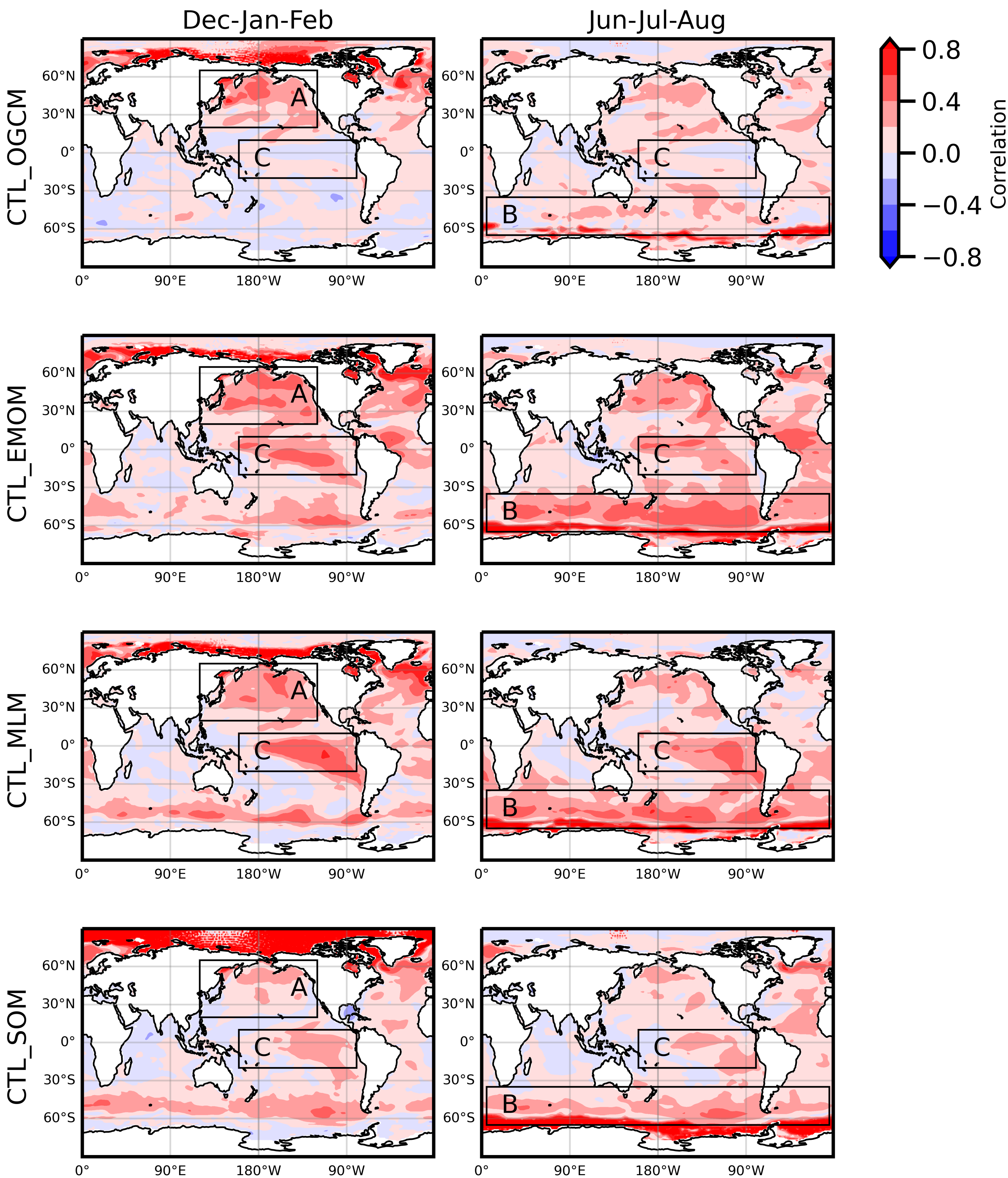

Dec-Jan-Feb
Jun-Jul-Aug
CTL_OGCM
CTL_EMOM
CTL_MLM
CTL_SOM
A
B
C
60°N
30°N
0°
30°S
60°S
0°
90°E
180°W
90°W
0.8
0.4
0.0
−0.4
−0.8
Correlation

Figure 7.

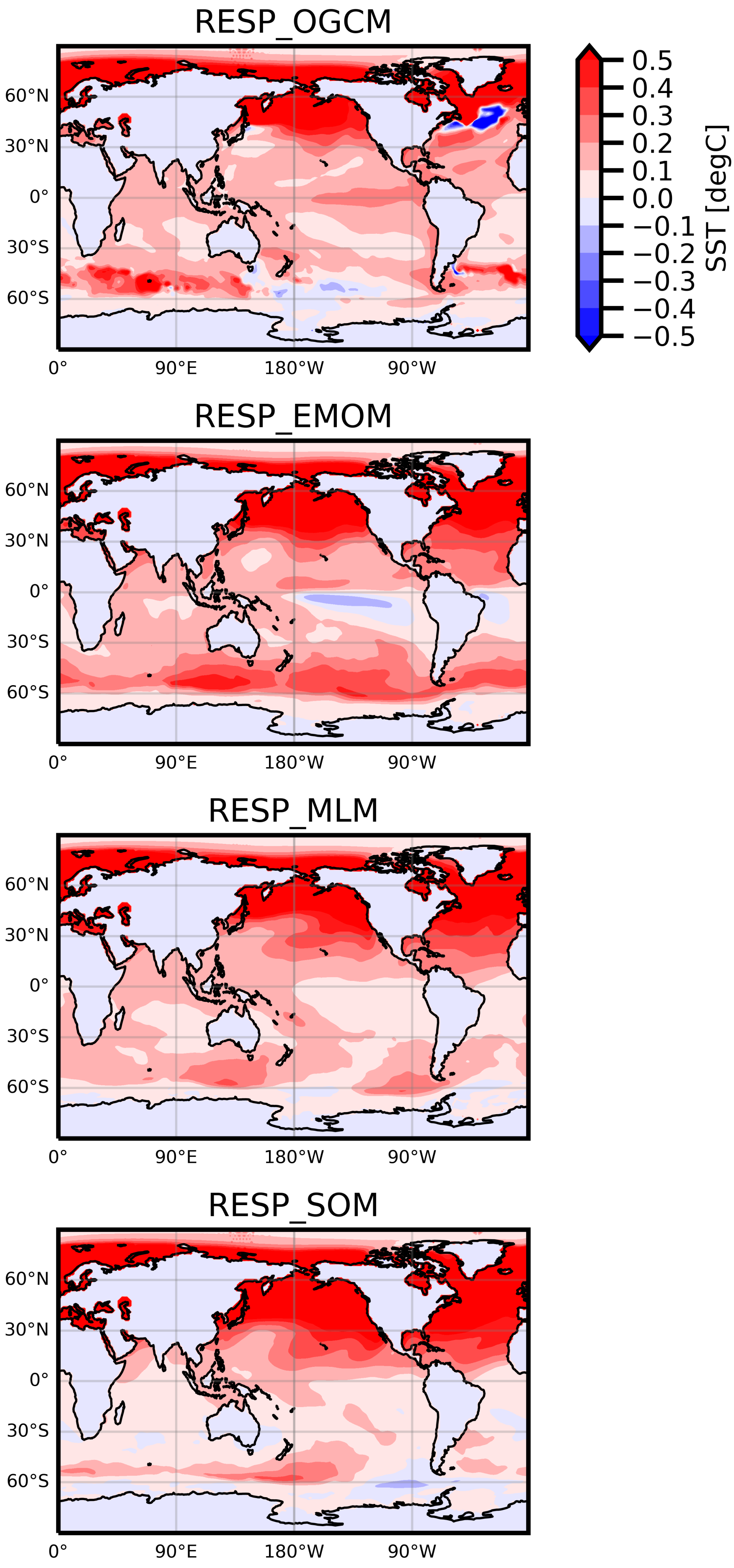
RESP_OGCM
RESP_EMOM
RESP_MLM
RESP_SOM
60°N
30°N
0°
30°S
60°S
0°
90°E
180°W
90°W
0.5
0.4
0.3
0.2
0.1
0.0
−0.1
−0.2
−0.3
−0.4
−0.5
SST [degC]

Figure 8.

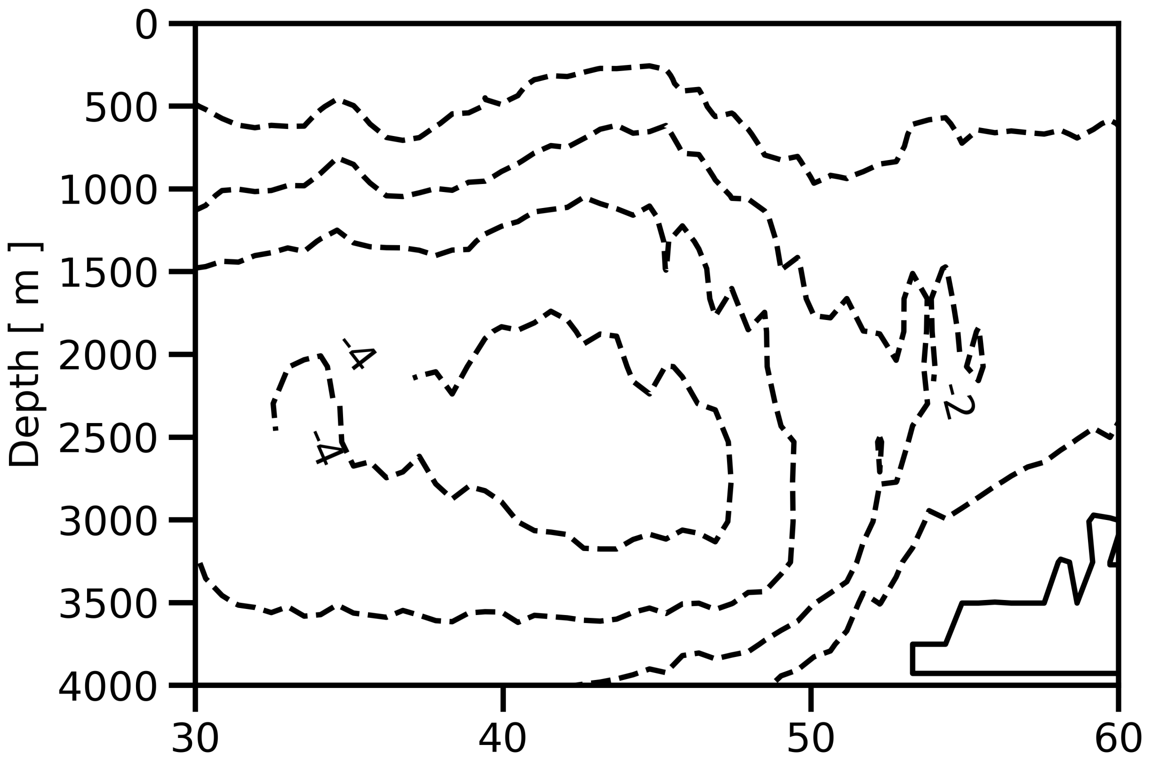
Depth [m]
0
500
1000
1500
2000
2500
3000
3500
4000
30
40
50
60
-4
-4
-2

Figure 9.

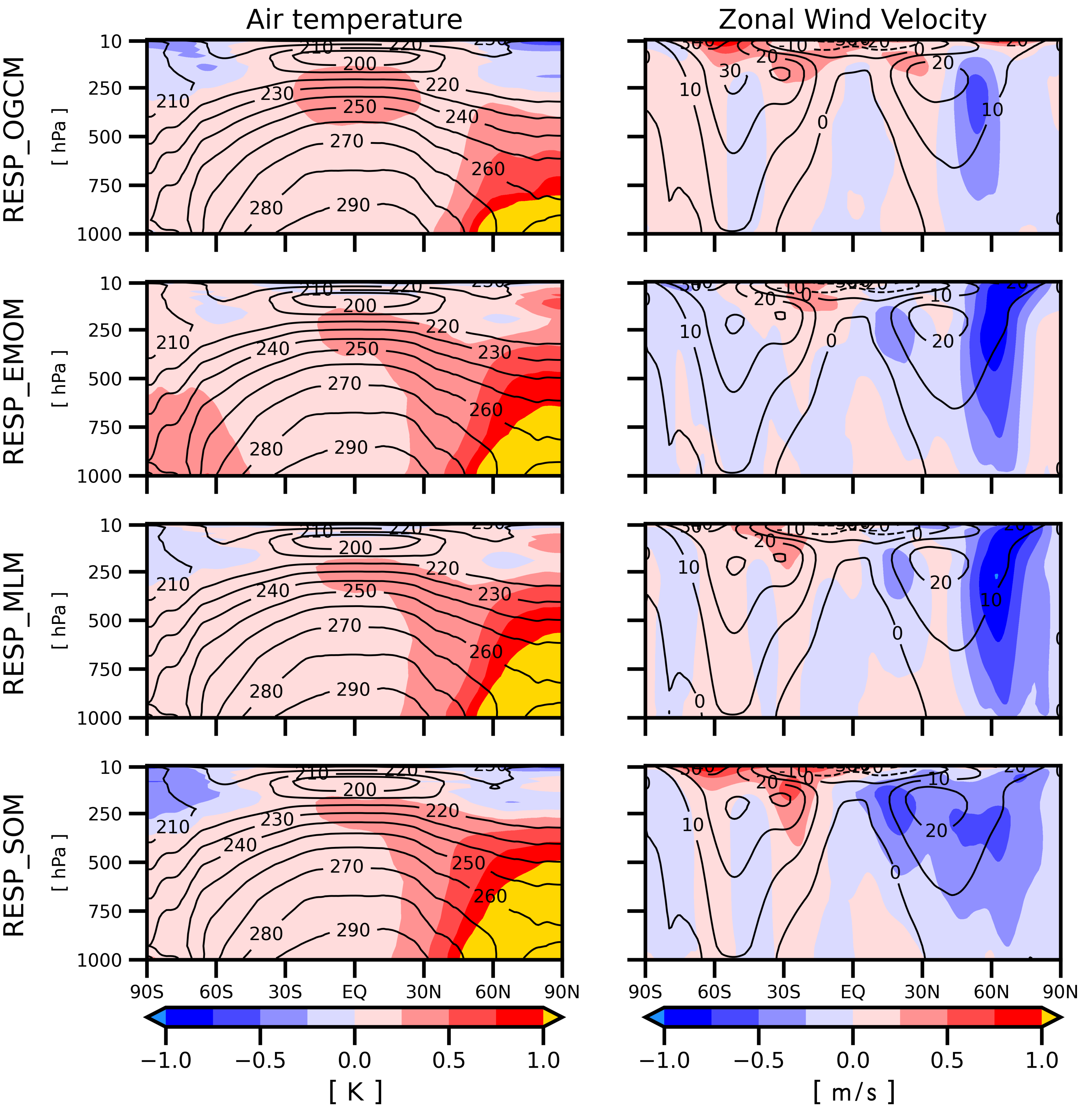

Air temperature
Zonal Wind Velocity
RESP_OGCM
RESP_EMOM
RESP_MLM
RESP_SOM
[hPa]
10
250
500
750
1000
90S
60S
30S
EQ
30N
60N
90N
−1.0
−0.5
0.0
0.5
1.0
[K]
[m/s]

Figure 10.

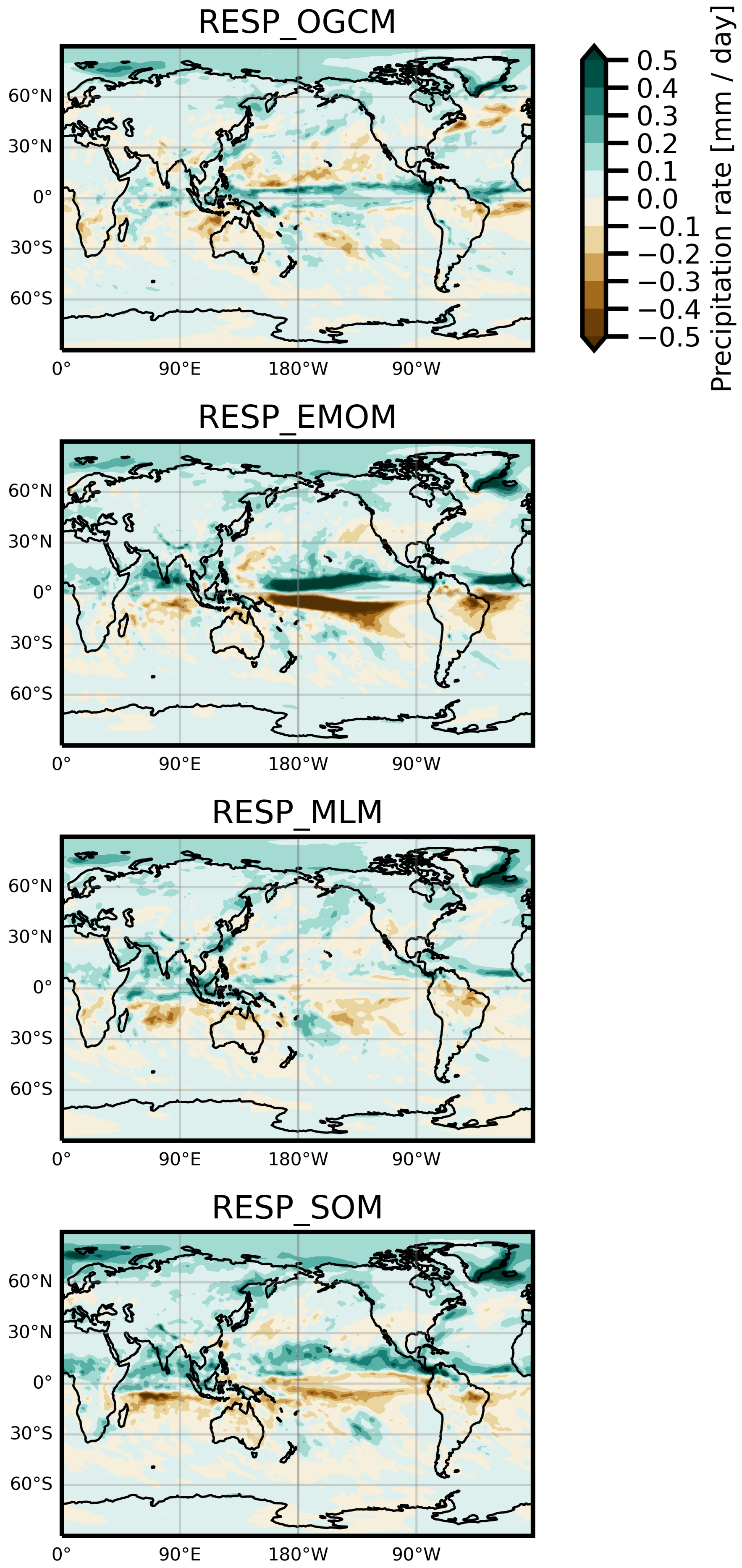
RESP_OGCM
RESP_EMOM
RESP_MLM
RESP_SOM
60°N
30°N
0°
30°S
60°S
0°
90°E
180°W
90°W
0.5
0.4
0.3
0.2
0.1
0.0
−0.1
−0.2
−0.3
−0.4
−0.5
Precipitation rate [mm / day]

Figure 11.

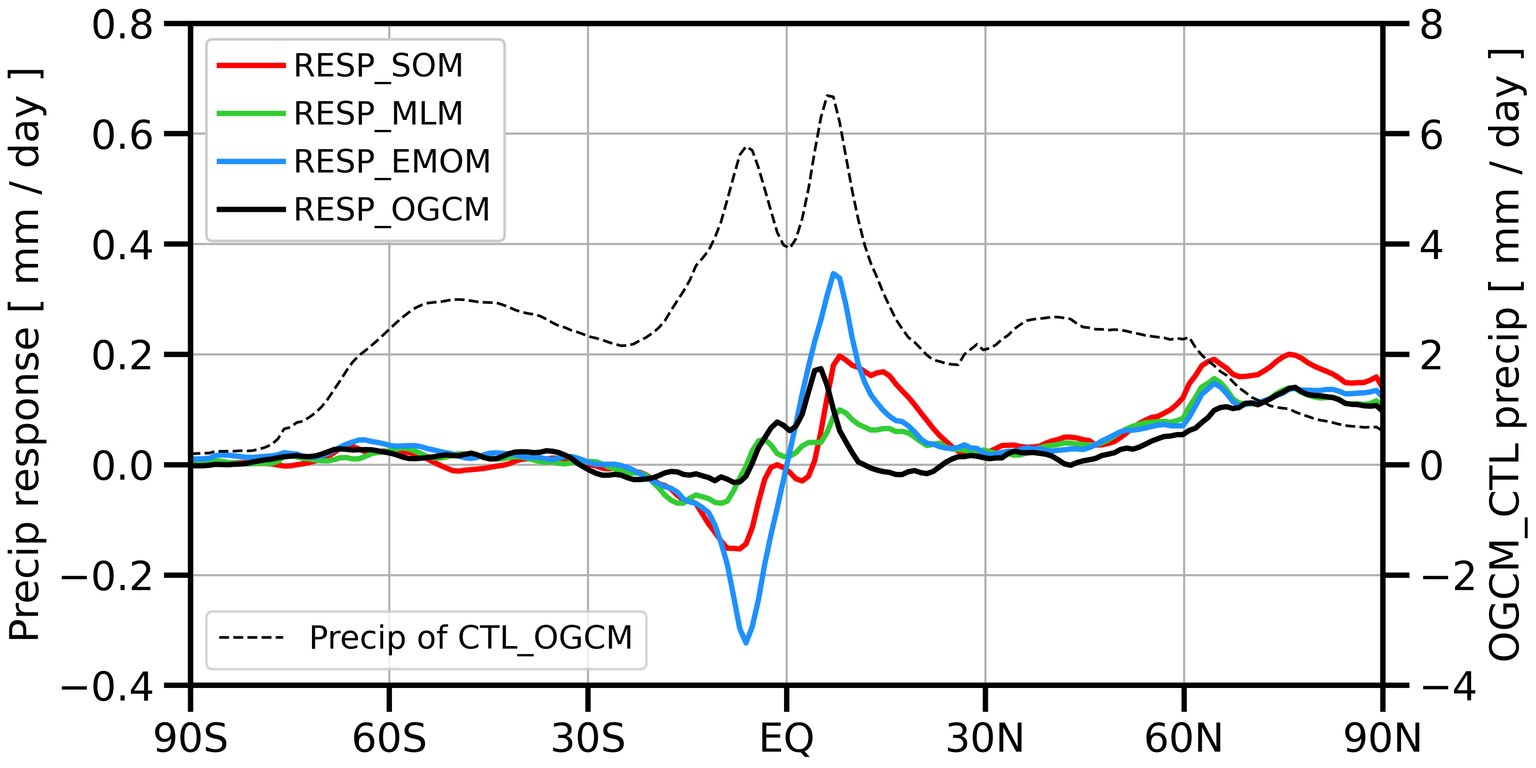

RESP_SOM
RESP_MLM
RESP_EMOM
RESP_OGCM
Precip of CTL_OGCM
Precip response [mm / day]
OGCM_CTL precip [mm / day]
0.8
0.6
0.4
0.2
0.0
−0.2
−0.4
8
6
4
2
0
−2
−4
90S
60S
30S
EQ
30N
60N
90N

Figure 12.

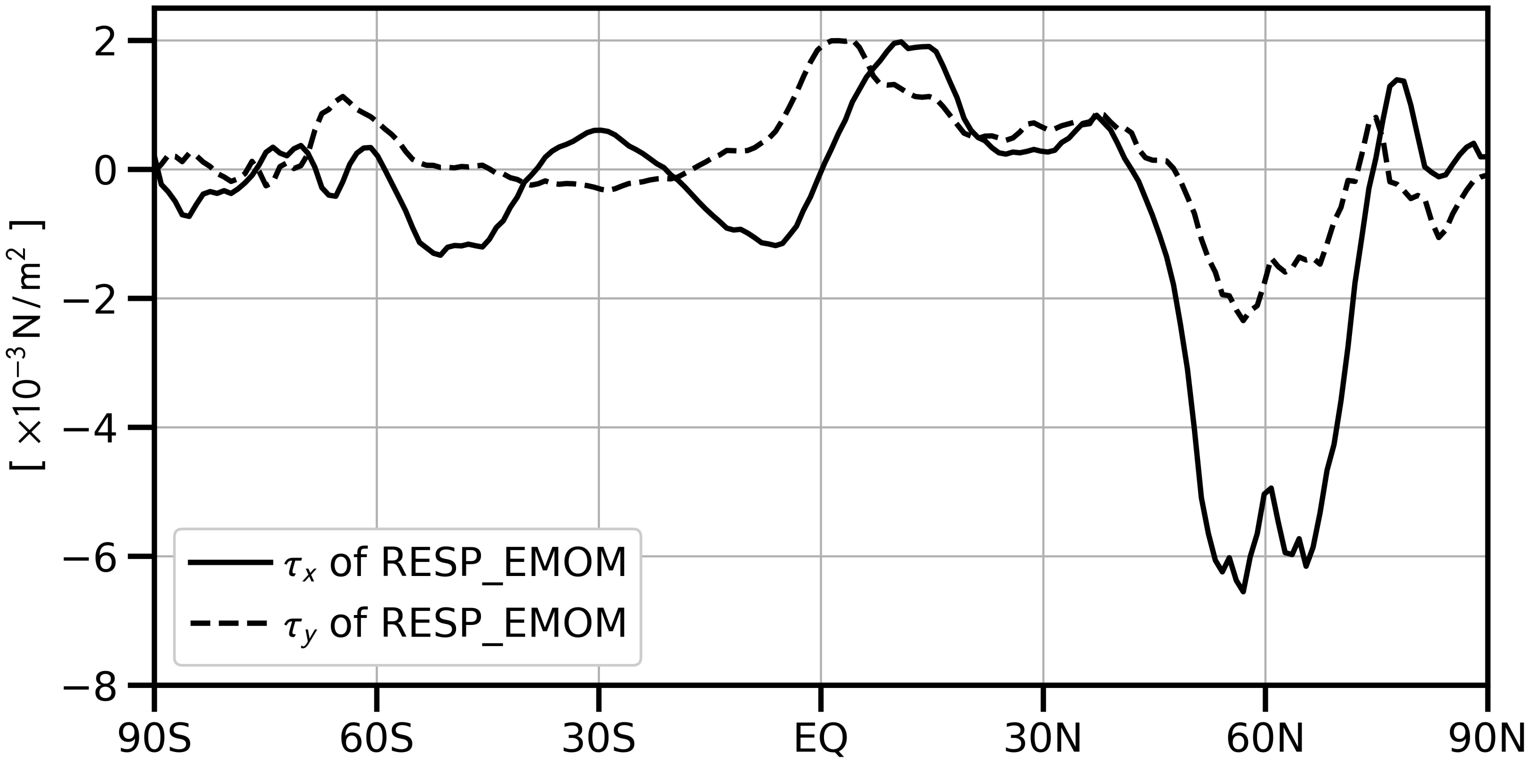

2
0
−2
−4
−6
−8
[×10^{-3}N/m^2]
90S
60S
30S
EQ
30N
60N
90N
τ_x of RESP_EMOM
τ_y of RESP_EMOM

Figure 13.

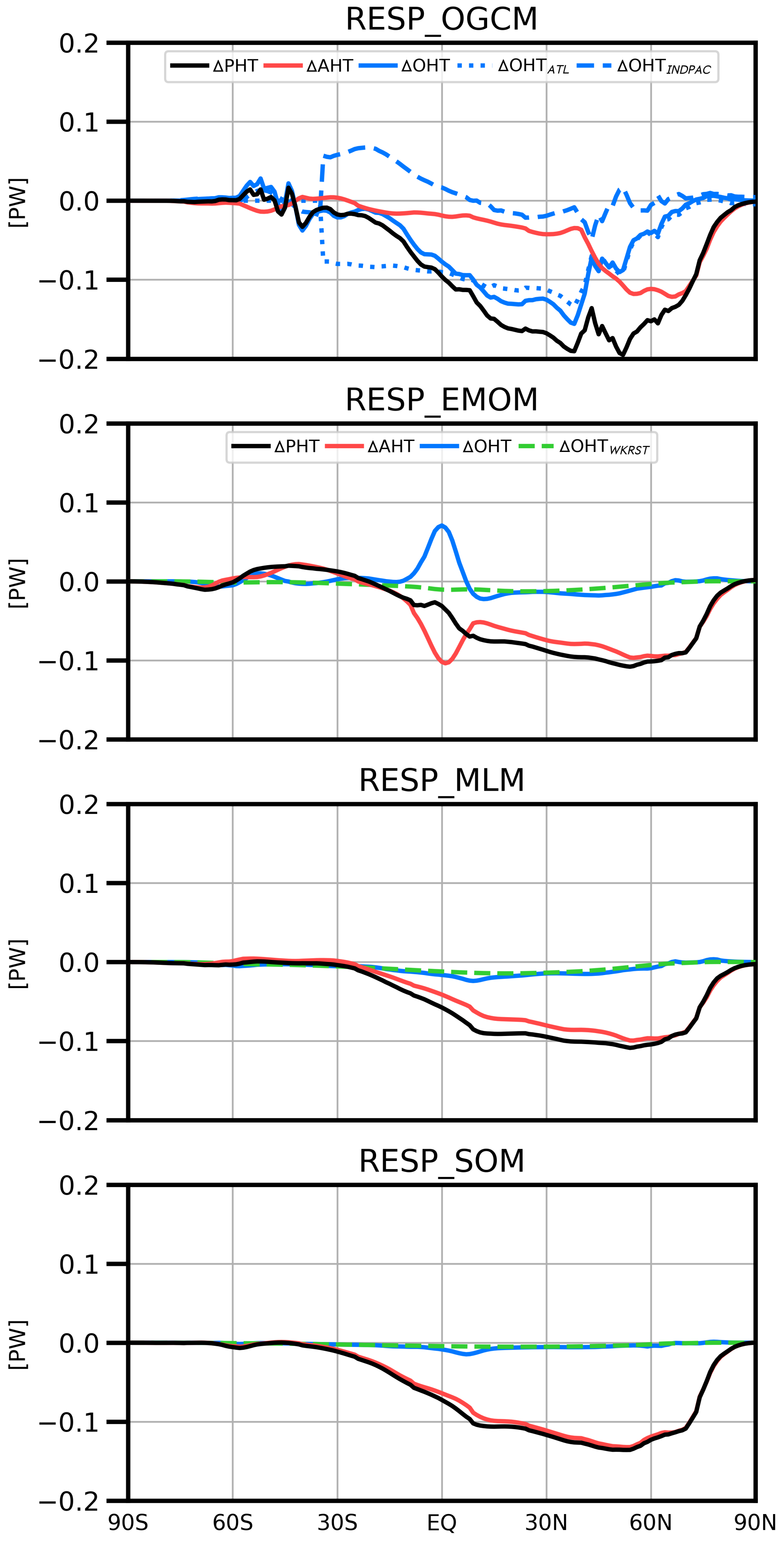

RESP_OGCM
ΔPHT
ΔAHT
ΔOHT
ΔOHT_ATL
ΔOHT_INDPAC
RESP_EMOM
ΔPHT
ΔAHT
ΔOHT
ΔOHT_WKRST
RESP_MLM
RESP_SOM
[PW]
0.2
0.1
0.0
−0.1
−0.2
90S
60S
30S
EQ
30N
60N
90N

Supporting Information for "A Hierarchy of Global Ocean Models Coupled to CESM1"

Tien-Yiao Hsu[1], Francois Primeau[1], and Gudrun Magnusdottir[1]

[1]University of California, Irvine, California, United States

Contents of this file

1. Figures S1 to S3.

Introduction This supporting information provides the following content:

1. Figure S1: The analysis plots showing the air-sea coupled-mode in the equator due to horizontal diffusion coefficient being too small.

2. Figure S2: The analysis plot of ocean mean temperature and AMOC strength time series that help determine the range of time selected to compute the mean of climate response in SIL.

3. Figure S3: The sea-ice thickness distribution of both CTL and SIL.

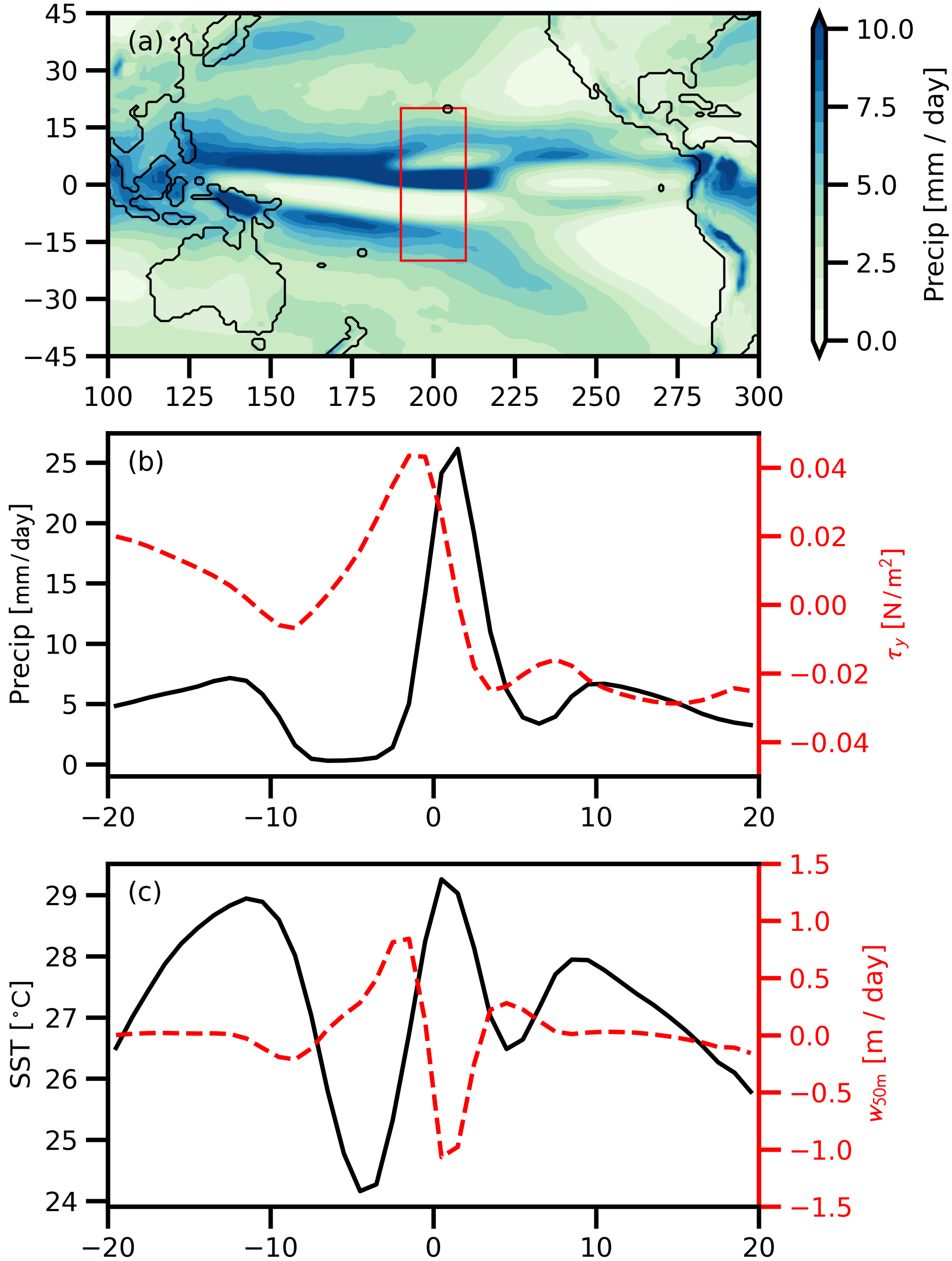

Figure S1. The annual mean values of year 30 of CTL_EMOM in which uniform $K_H = 1500\,\mathrm{m}^2\,/\,\mathrm{s}$ is used. (a) shows the precipitation map of tropical Pacific. (b) shows the zonal mean precipitation (left axis, solid black) and zonal mean meridional wind stress (right axis, red dashed, positive means that wind blows northward) of the regions boxed in (a). (c) is the same as (b) but for SST and oceanic 50-m vertical velocity.

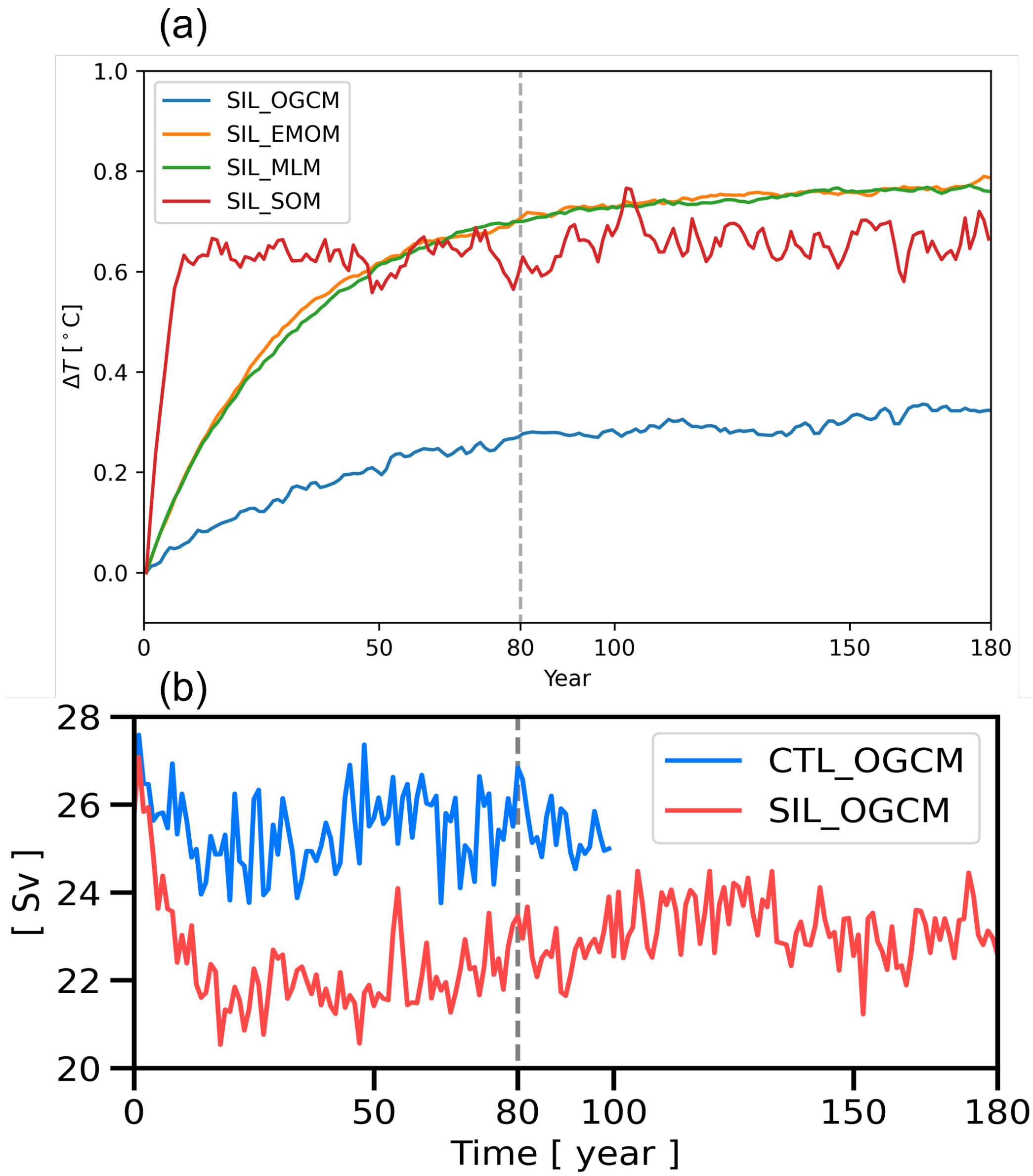

Figure S2. (a) The temporal evolution of mean ocean temperature in top 503.7m in SIL relative to the beginning year of each trajectory. Time window year 80–180 during which SIL data are used for statistics is labeled. Notice that the mean ocean thickness of SOM is about 100 meters so there are more temporal fluctuations. (b) The temporal evolution of AMOC intensity measured in Sv.

Figure S3. The blue shading shows the regions where the annual mean sea-ice thickness is greater than 1 m in control run. The red shading is the same but with data derived from RCP 8.5 year 2081–2100 of CMIP5.